T cell protein tyrosine phosphatase protects intestinal barrier function by restricting epithelial tight junction remodeling

Ronald R. Marchelletta,[1] Moorthy Krishnan,[2] Marianne R. Spalinger,[2] Taylaur W. Placone,[1] Rocio Alvarez,[2] Anica Sayoc-Becerra,[2] Vinicius Canale,[2] Ali Shawki,[2] Young Su Park,[1] Lucas H.P. Bernts,[1] Stephen Myers,[1] Michel L. Tremblay,[3] Kim E. Barrett,[1] Evan Krystofiak,[4] Bechara Kachar,[4] Dermot P.B. McGovern,[5] Christopher R. Weber,[6] Elaine M. Hanson,[1] Lars Eckmann,[1] and Declan F. McCole[2]

[1]Division of Gastroenterology, Department of Medicine, School of Medicine, University of California, San Diego, La Jolla, California, USA. [2]Division of Biomedical Sciences, School of Medicine, University of California, Riverside, Riverside, California, USA. [3]Department of Biochemistry and Goodman Cancer Research Centre, Faculty of Medicine and Health Sciences, McGill University, Montréal, Québec, Canada. [4]National Institute on Deafness and Other Communication Disorders, NIH, Bethesda, Maryland, USA. [5]F. Widjaja Foundation Inflammatory Bowel and Immunobiology Research Institute, Cedars-Sinai Medical Center, Los Angeles, California, USA. [6]Department of Pathology, University of Chicago, Chicago, Illinois, USA.

Genome-wide association studies revealed that loss-of-function mutations in protein tyrosine phosphatase non-receptor type 2 (*PTPN2*) increase the risk of developing chronic immune diseases, such as inflammatory bowel disease (IBD) and celiac disease. These conditions are associated with increased intestinal permeability as an early etiological event. The aim of this study was to examine the consequences of deficient activity of the *PTPN2* gene product, T cell protein tyrosine phosphatase (TCPTP), on intestinal barrier function and tight junction organization in vivo and in vitro. Here, we demonstrate that TCPTP protected against intestinal barrier dysfunction induced by the inflammatory cytokine IFN-γ by 2 mechanisms: it maintained localization of zonula occludens 1 and occludin at apical tight junctions and restricted both expression and insertion of the cation pore-forming transmembrane protein, claudin-2, at tight junctions through upregulation of the inhibitory cysteine protease, matriptase. We also confirmed that the loss-of-function *PTPN2* rs1893217 SNP was associated with increased intestinal claudin-2 expression in patients with IBD. Moreover, elevated claudin-2 levels and paracellular electrolyte flux in TCPTP-deficient intestinal epithelial cells were normalized by recombinant matriptase. Our findings uncover distinct and critical roles for epithelial TCPTP in preserving intestinal barrier integrity, thereby proposing a mechanism by which *PTPN2* mutations contribute to IBD.

Introduction

The epithelial barrier is essential for intestinal homeostasis and is critical in preserving intestinal functions such as maintaining ionic balance, establishing a protective layer between the intestinal microbiota and the mucosa, and absorbing water and nutrients (1, 2). Disruption of apical tight junctions increases paracellular permeability to electrolytes and macromolecules, such as dietary antigens and bacterial products (3). This can induce activation of the mucosal immune system, resulting in inflammation and tissue damage (1, 4, 5). Moreover, loss of barrier integrity contributes to diarrheal and inflammatory symptoms in patients with inflammatory bowel disease (IBD; refs. 1, 6). While the 2 subtypes of IBD, Crohn's disease (CD) and ulcerative colitis (UC), display several distinct pathological features, they both feature a dysfunctional intestinal barrier early in disease, before the onset of gross inflammation (5, 7). Thus, a compromised epithelial barrier is a hallmark of IBD pathogenesis. While initially presumed to be entirely a consequence of elevated inflammatory cytokine expression, increased intestinal permeability actually precedes inflammation in animal models of colitis and serves as a predictor of disease onset in first-degree relatives and of relapse in patients with IBD (8–13). Cumulatively, this suggests that reduced epithelial barrier function plays an essential early role in IBD pathogenesis. However, while increased permeability by itself is insufficient to cause colitis in animal models, it is required for intestinal inflammation (8, 9, 14). The exact mechanisms involved in the initiation of barrier dysfunction, and how they interact with other IBD risk factors, remain elusive.

SNPs in over 200 gene loci are associated with increased IBD risk (15, 16). One such gene, protein tyrosine phosphatase non-receptor type 2 (*PTPN2*), is associated with CD, UC, and other chronic immune conditions, including celiac disease, type 1 diabetes, and rheumatoid arthritis, all of which exhibit increased intestinal permeability early in disease (15–19). The disease-associated SNPs give rise to loss-of-function mutations in the *PTPN2* product, T cell protein tyrosine phosphatase (TCPTP; refs. 20, 21).

TCPTP belongs to a family of protein tyrosine phosphatases that share a conserved catalytic domain (22). TCPTP is ubiquitously expressed and is essential for normal cellular function in many

Conflict of interest: The authors have declared that no conflict of interest exists.

Submitted: March 31, 2020; **Accepted:** July 22, 2021; **Published:** September 1, 2021.
Reference information: *J Clin Invest*. 2021;131(17):e138230.
https://doi.org/10.1172/JCI138230.

cell types, including hematopoietic and epithelial cells (23–25). TCPTP dephosphorylates — thereby deactivating — members of the janus kinase (JAK) and signal transducer and activator of transcription (STAT) pathways activated by interferon-γ (IFN-γ; i.e., JAK1, STAT1, -3) and other cytokines (JAK3, STAT5, -6; ref. 26). Dysregulated STAT signaling can contribute to IBD pathogenesis while STAT3 is also an IBD candidate gene (27, 28). Importantly, IFN-γ increases TCPTP expression as part of a negative feedback loop to restrict IFN-γ signaling (25).

Building on our observations that TCPTP promotes intestinal epithelial barrier properties in vitro (25, 29, 30), we now identify that TCPTP protects the intestinal epithelial barrier in vivo and in vitro through bimodal restriction of the claudin-2 cation pore, and preventing mislocalization of occludin and zonula occludens proteins at the apical tight junction, thus reducing permeability to electrolytes and macromolecules. These data confirm epithelial TCPTP as a key regulator of barrier function and suggest a mechanism by which *PTPN2* loss-of-function mutations contribute to chronic inflammatory diseases, such as IBD.

Results

Loss of TCPTP compromises intestinal barrier function. TCPTP loss compromises epithelial barrier function in vitro (25, 29, 30). To determine whether this occurs in vivo, we assessed intestinal barrier function in whole-body *Tcptp*-deficient mice. To precede the described onset of systemic inflammation in *Tcptp*-knockout mice, intestinal tissues were isolated from 18- to 21-day-old *Tcptp* wild-type (WT), heterozygous (HET), and homozygous constitutive knockout (KO) mice and probed for TCPTP expression (31, 32). As expected, KO mice exhibited loss of TCPTP expression in the ileum, cecum, and proximal and distal colon (Supplemental Figure 1A; supplemental material available online with this article; https://doi.org/10.1172/JCI138230DS1). Concomitantly, phosphorylation of the TCPTP substrates JAK3 and STAT1 was increased (Supplemental Figure 1, B–D), while KO mice also displayed body weight loss and splenomegaly (Supplemental Figure 1, E and F). In vivo intestinal permeability to 4 kDa FITC-dextran (FD4) was significantly increased in HET mice and further increased in KO mice (~4-fold) compared with WT cohoused littermates (Figure 1A). Serum rhodamine B-dextran 70 kDa (RD70) flux was not significantly increased in HET or KO mice compared with WT littermates, indicating that "unrestricted" and tight junction–independent permeability was not a factor in the elevated permeability to FD4 (Figure 1B). Histological analysis (H&E staining) revealed an intact epithelium in small and large intestine in KO and HET mice (Figure 1C), although a decrease in colon length and increased crypt depths were seen in the cecum and proximal colon, but not distal colon, of KO mice (Figure 1, D and E). Ex vivo electrophysiological analyses of transepithelial electrical resistance (TER) (which measures resistance to the passive flux of electrolytes, such as sodium) and FD4 flux across isolated small and large intestinal tissues mounted in Ussing chambers revealed regional differences (Figure 2, A–J). Significant decreases in TER occurred in the distal ileum (Figure 2B) and cecum from HET and KO mice (Figure 2C), while KO mice also showed significantly reduced TER in the distal colon (Figure 2E). Mucosal FD4 permeability was significantly increased in the cecum and proximal colon from *Tcptp*-KO mice (Figure 2, H and I). Cumulatively, these data demonstrate a compromised epithelial barrier with increased tight junction–dependent electrolyte flux and macromolecule permeability in specific gut segments of *Tcptp*-deficient mice.

TCPTP loss promotes intestinal epithelial tight junction remodeling in vivo. Intestinal epithelial cells (IECs) isolated from *Tcptp*-deficient mice showed normal expression of the integral transmembrane tight junction protein, occludin, and the junction peripheral membrane scaffolding protein, zonula occludens 1 (ZO-1; Figure 3, A–D). However, the normally clear focal localization of ZO-1 (shown in green) and occludin (shown in red) at apical tight junctions was disrupted in KO mice, which instead showed more diffuse staining in the apical and subapical membranes (Figure 3E).

TNF-α/IFN-γ–induced internalization of tight junction proteins, and increased paracellular permeability, require phosphorylation of the myosin light chain (MLC) protein (33–35). Immunostaining of the colon and Western blotting of IECs isolated from the ileum, cecum, and colon showed increased MLC activation (phosphorylated Ser19) in KO mouse epithelium (Figure 3, F–H). Overall, these data indicate that loss of TCPTP leads to tight junction remodeling and increased MLC phosphorylation, which is consistent with the elevated FD4 permeability observed in vivo and ex vivo (c.f. Figure 2).

Tcptp-deficient mice exhibit elevated mucosal inflammatory cytokine profiles. We next determined if TCPTP loss altered regional expression of mucosal cytokines capable of altering barrier function. By multiplex expression analysis, we identified a gene-titrated increase in IFN-γ in HET mice, and significantly higher levels of IFN-γ, TNF-α, and IL-6 in the colon of KO mice, compared with WT and HET mice (Supplemental Figure 2, A–C). Ileal cytokine levels were below the level of detection. IL-22 was significantly elevated in the distal colon of KO mice versus WT (Supplemental Figure 2D). The Th2 cytokines IL-5 and IL-4 were significantly decreased in KO mouse cecum and distal colon, respectively (Supplemental Figure 2, E and F), whereas *Il13* was unchanged (Supplemental Figure 3A). Serum cytokine analysis showed increased IFN-γ and TNF-α levels in KO mice (Supplemental Figure 3, B and C), both of which are elevated in IBD, particularly CD (31, 32, 36, 37). In addition, serum levels of IL-5 were higher in KO mice despite reduced expression in intestinal mucosal tissues (Supplemental Figure 3D). No change was observed in serum levels of IL-4 or IL-6 between genotypes (Supplemental Figure 3, E and F). These data identify increased serum inflammatory cytokines in KO mice but also discrete changes in intestinal protein levels of mucosal Th1- and Th2-associated cytokines.

Tcptp-deficient mice exhibit altered tissue lymphocyte and myeloid populations. To identify the source of inflammatory cytokines, we performed flow cytometric analysis of immune cell populations in the cecum, colon, mesenteric lymph nodes, and spleen (Supplemental Figure 4). We identified tissue-specific increases in IFN-γ$^+$ CD4$^+$ and CD8$^+$ T cells, TNF-α$^+$CD8$^+$ T cells, and IL-22$^+$CD4$^+$ T cells in KO mice (Supplemental Figure 5). Decreases in IL-17$^+$CD4$^+$ T cells were observed in the cecum, colon, and lymph nodes, while IL-4$^+$CD4$^+$ and IL-10$^+$ Tregs were also reduced in KO mice, although there was no overall decrease in Treg numbers in any tissue (Supplemental Figure 5). Myeloid cell characterization showed no change in overall murine Ly6C^{hi} or Ly6C^{lo} monocytes or

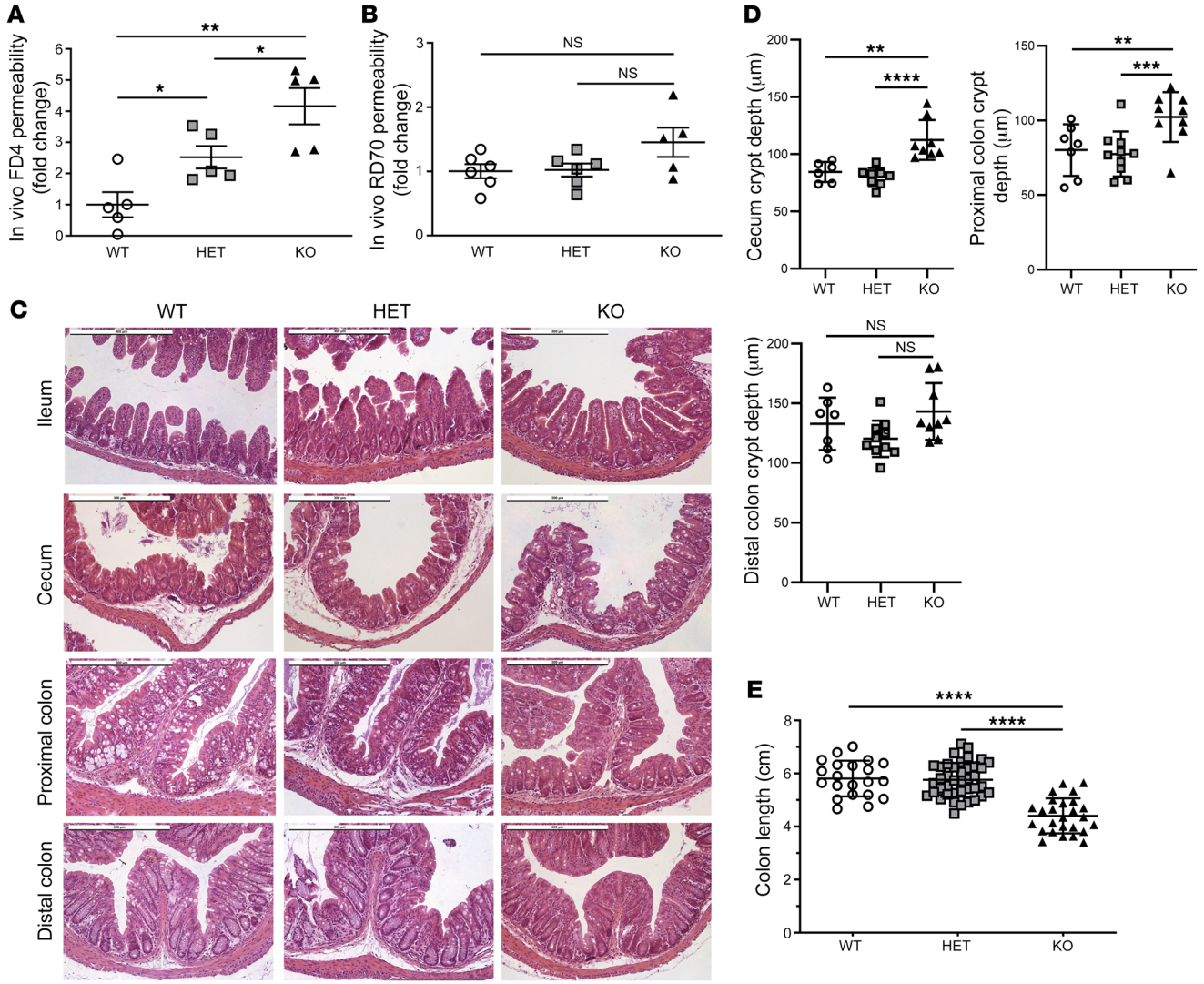

Figure 1. *Tcptp*-deficient mice display increased intestinal permeability in vivo. (**A**) FITC-dextran 4 kDa (FD4) and (**B**) rhodamine 70 kDa (RD70) were administered by oral gavage to *Tcptp* WT, HET, and KO mice aged 18–21 days. Serum was collected after 5 hours and FD4 and RD70 concentration determined. (**C**) H&E staining of intestinal tissues from *Tcptp* WT, HET, and KO mice (18–21 days old) shows that an intact epithelium is retained in *Tcptp*-deficient mouse intestine. Blinded histological scoring (not shown) by a pathologist indicated no substantive difference in histology between genotypes ($n = 4$). Scale bars: 300 μm. (**D**) Crypt depth in large intestinal regions (cecum, proximal and distal colon) from *Tcptp* WT, HET, and KO mice was quantified and expressed in micrometers ($n = 6$–10). (**E**) Isolated colon length from *Tcptp* WT ($n = 21$), HET ($n = 40$), and KO ($n = 26$) mice was measured and expressed in centimeters. Data are expressed as mean ± SD. Statistical significance was calculated by 1-way ANOVA and Student-Newman-Keuls posttest. $^*P < 0.05$; $^{**}P < 0.01$; $^{***}P < 0.001$; $^{****}P < 0.0001$.

the relative abundance of dendritic cells (Supplemental Figure 6, A–C). The proportion of macrophages was increased in KO mouse cecum and colon (Supplemental Figure 6D). In KO mice, all tissues showed a larger proportion of M1-like ($MHCII^{hi}CD206^{lo}$) macrophages and decreased abundance of M2-like ($MHCII^{lo}CD206^{hi}$) macrophages (Supplemental Figure 6, E and F). Thus, global TCPTP loss provokes increased intestinal Th1 T lymphocytes and proinflammatory macrophage polarization.

Intestinal epithelial-specific TCPTP loss in vivo predisposes to increased intestinal permeability. To distinguish between immune cell and epithelial contributions to the permeability defects in *Tcptp*-deficient mice, we generated tamoxifen-inducible (TMX-inducible) epithelial TCPTP-KO mice ($Ptpn2^{\Delta IEC}$; see Supplemental Figure 7). In vivo assessment of FD4 permeability showed no difference between adult $Ptpn2^{\Delta IEC}$ and $Ptpn2^{fl/fl}$ control mice following TMX-induced epithelial *Ptpn2* deletion (Figure 4A). However, ex vivo analysis showed significant changes in underlying permeability with reduced TER (Figure 4, B–D) and increased FD4 flux (Figure 4, E–G) in the cecum and proximal colon — but not distal colon — of $Ptpn2^{\Delta IEC}$ mice. We next determined the effect of in vivo cytokine challenge (24 hours) to $Ptpn2^{\Delta IEC}$ mice and $Ptpn2^{fl/fl}$ mice on regional barrier function in colonic tissues subsequently isolated and mounted in Ussing chambers. IL-6 induced a significant decrease in TER in the cecum (Figure 4B) and distal colon (Figure 4D) of $Ptpn2^{\Delta IEC}$ mice, while it exacerbated the underlying defect in the proximal colon (Figure 4C). IL-6 also increased

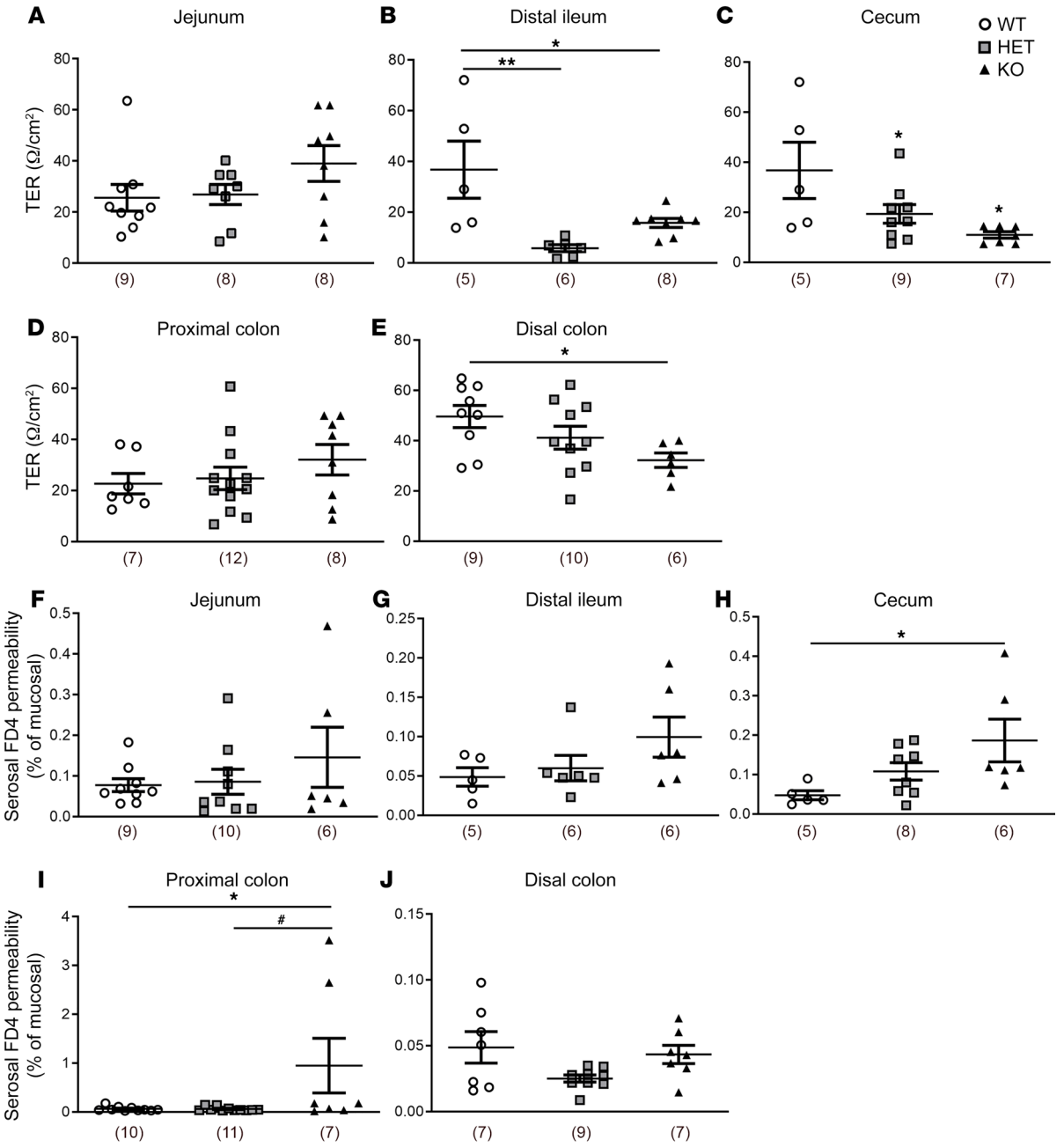

Figure 2. *Tcptp*-deficient mice display regional variations in macromolecule and electrolyte intestinal permeability ex vivo. In Ussing chambers, mucosal transepithelial electrical resistance (TER) (**A**–**E**) and ex vivo FD4 permeability (**F**–**J**) were measured across isolated (**A** and **F**) jejunum, (**B** and **G**) distal ileum, (**C** and **H**) cecum, (**D** and **I**) proximal colon, and (**E** and **J**) distal colon (n = 5–11). Data are expressed as mean ± SEM. Numbers of mice shown in parentheses. Comparisons between groups were by 1-way ANOVA and Student-Newman-Keuls posttest. $^{*}P < 0.05$, and $^{**}P < 0.01$ vs. WT; $^{\#}P < 0.05$ vs. HET.

the constitutive elevation in FD4 permeability in *Ptpn2*$^{\Delta IEC}$ mouse cecum, but no difference was found in colonic regions (Figure 4E). IFN-γ or TNF-α significantly reduced TER in the cecum and proximal colon, while IFN-γ but not TNF-α increased FD4 permeability in the cecum and proximal colon (Figure 4, E and F). IFN-γ and TNF-α in combination significantly reduced TER in all 3 regions and increased FD4 flux in cecum and proximal colon. Of note, no underlying increase in FD4 permeability was found in distal colon, and this was not significantly altered by cytokine treatment (Figure 4G). Ex vivo tissue viability was confirmed by electrogenic transport responses to Ca^{2+} and cAMP stimuli that were unaffected in the different genotypes (Supplemental Figure 8). Confirmation of in vivo IFN-γ–, IL-6– or TNF-α–induced signaling was generated by Western blotting of IECs isolated from cytokine-treated mice, which showed elevated STAT1, STAT3, and NF-κB (p65) phosphorylation, respectively, and this was further elevated in *Ptpn2*$^{\Delta IEC}$ mice (Supplemental Figure 9, A–D). In agreement with in vitro studies, we observed that loss of epithelial TCPTP in vivo was sufficient to increase expression of the cation pore-forming tight junction protein, claudin-2 (Supplemental Figure 9, A–D, and

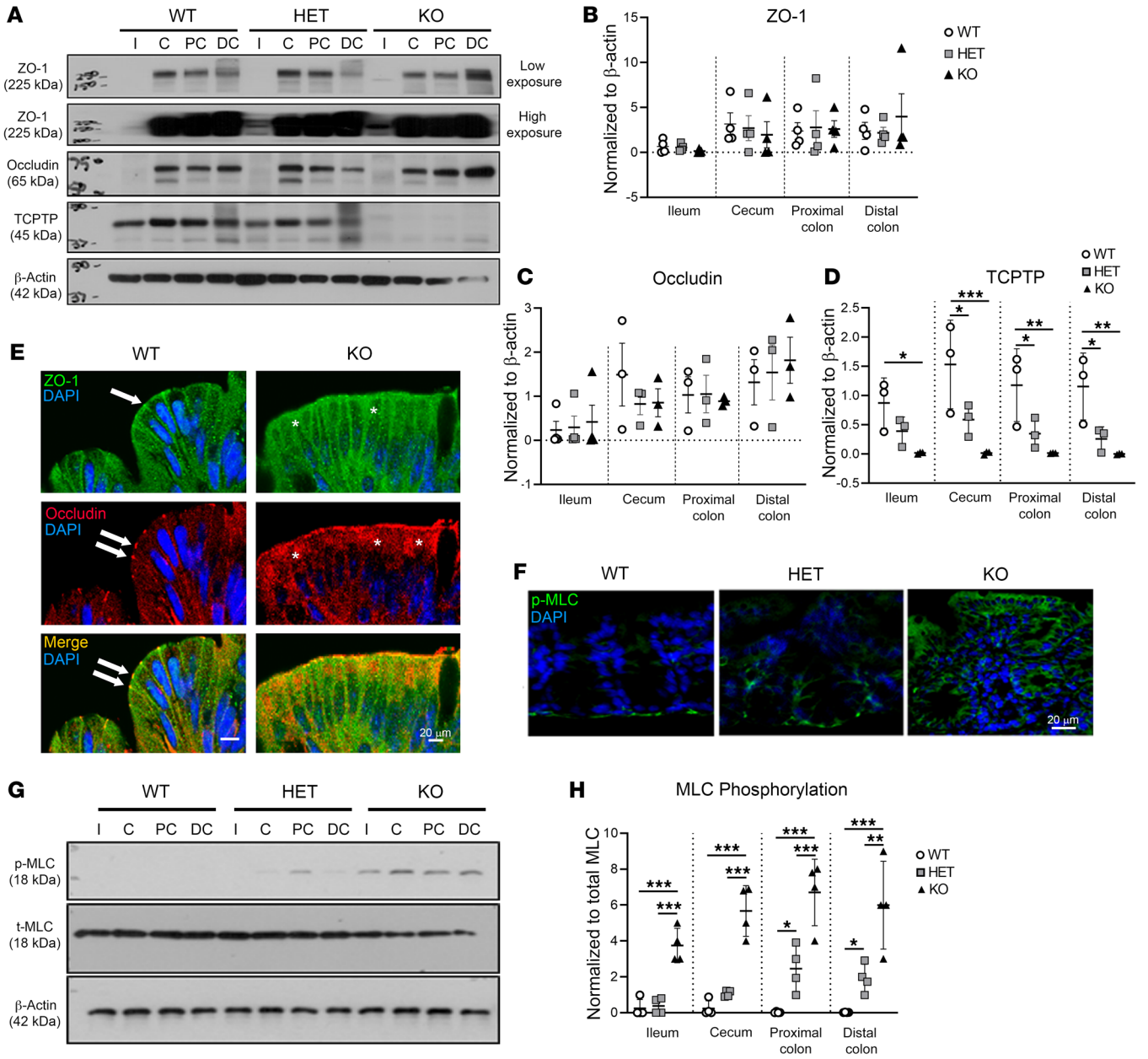

Figure 3. Loss of TCPTP promotes intestinal epithelial tight junction protein remodeling in vivo. (**A**) Epithelial cells from ileum (I), cecum (C), proximal colon (PC), and distal colon (DC) were isolated from *Tcptp* WT, HET, and KO mice. Cells were lysed and probed by Western blotting for expression of tight junction proteins ZO-1 and occludin as well as TCPTP and β-actin. Insertion of cropped bands from ileal samples is denoted by black lines. (**B**) Densitometric analysis of ZO-1, (**C**) Occludin, and (**D**) TCPTP expression normalized to β-actin from *Tcptp* WT, HET, and KO mouse intestinal epithelium (n = 3–4). (**E**) Representative confocal micrographs of ZO-1 and occludin localization at tight junctions (arrows) in proximal colon from *Tcptp* WT and KO mice (n = 3). Asterisks show diffuse ZO-1 and occludin staining in *Tcptp*-KO mouse colon. (**F**) Myosin light chain (MLC) phosphorylation (Ser19) in proximal colon from WT, HET, and KO mice. (**G**) Western blot and (**H**) densitometric analysis of MLC phosphorylation in isolated IECs from *Tcptp* WT, HET, and KO mice normalized to total MLC (n = 3–4). Data expressed as mean ± SD. Statistical significance was calculated by 1-way ANOVA and Student-Newman-Keuls posttest. $^*P < 0.05$; $^{**}P < 0.01$; and $^{***}P < 0.001$.

ref. 30). This was further increased by IL-6 and IFN-γ (alone or in combination with TNF-α) but not TNF-α alone. These data demonstrate: (a) loss of TCPTP in IECs induced region-specific intestinal permeability defects that were not revealed by global assessment of intestinal permeability in vivo; (b) IEC loss of TCPTP increased susceptibility to cytokine-induced permeability defects; and (c) this susceptibility was cytokine and region specific. Overall, these data confirm that loss of TCPTP expression in IECs alone was sufficient to compromise intestinal epithelial barrier function.

A loss-of-function PTPN2 mutant promotes cytokine-induced tight junction remodeling and increased permeability. To identify if a TCPTP loss-of-function mutation can precipitate tight junction reorganization, we generated a serine substitution of the cysteine at position 216 of the 45 kDa TCPTP isoform (TC45), the key site of

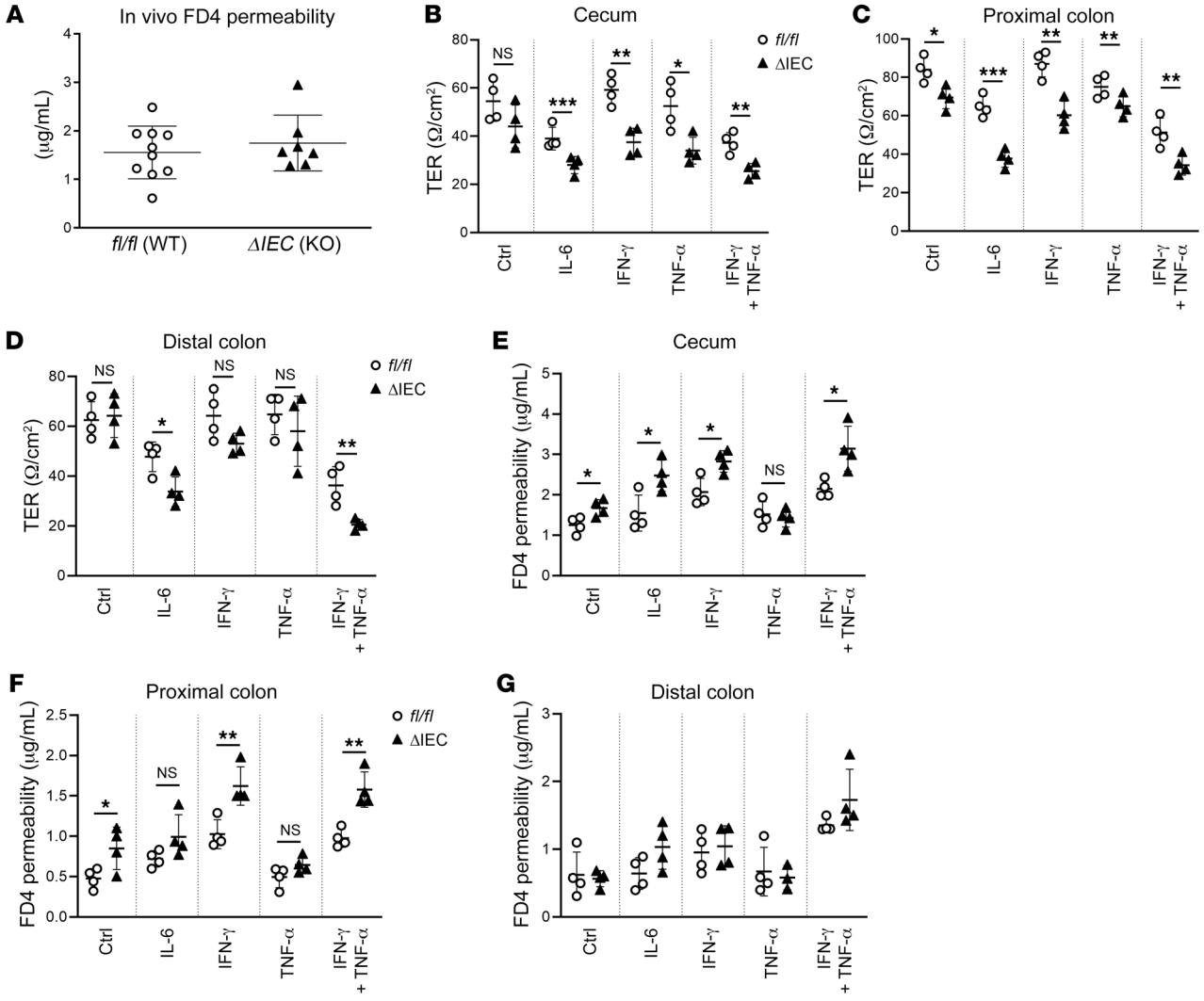

Figure 4. In vivo and ex vivo intestinal permeability measurements in cytokine-treated *Ptpn2*$^{\Delta IEC}$ KO mice. (**A**) FD4 was administered by oral gavage to *Ptpn2*$^{\Delta IEC}$ and *Ptpn2*$^{fl/fl}$ control mice. Serum was collected after 5 hours and FD4 concentration determined (n = 7–10). Mice were injected i.p. with IL-6, IFN-γ, TNF-α, or IFN-γ + TNF-α for 24 hours prior to tissue isolation and mounting in Ussing chambers. TER and FD4 permeability were measured in (**B** and **E**) cecum, (**C** and **F**) proximal colon, and (**D** and **G**) distal colon (n = 4). Data are expressed as mean ± SD. Comparisons between genotypes and within treatment groups were by unpaired 2-tailed Student's t test. *$P < 0.05$; **$P < 0.01$; ***$P < 0.001$.

TCPTP enzymatic activity and one with clinical relevance (24, 38). This C216S-TC45 construct with a hemagglutinin (HA) tag, under a doxycycline-inducible tetracycline repressor protein (TetR) promoter (Tet-On), was transfected into HCA-7 IECs. Doxycycline treatment induced expression of the HA-tagged TCPTP (Supplemental Figure 10A and Figure 5A). Reduced cellular TC45 enzymatic activity was confirmed following IFN-γ treatment of C216S IECs (+DOX induction), which significantly increased STAT1 phosphorylation above control vector–transfected IECs (Figure 5, B and C). Induction of C216S-TC45 expression was sufficient to cause functional disruption of tight junctions (reduced TER and increased FD4 permeability) that was further accentuated by IFN-γ (Figure 5, D and E). IFN-γ treatment of C216S-TC45–transfected cells also disrupted tight junction composition and decreased levels of ZO-1 and occludin in IEC membranes (Figure 5, F and G), indicative of the "leak pathway" barrier defect. ZO-1/occludin, and ZO-1/claudin-4, colocalization at IEC junctions was significantly decreased in IFN-γ–treated C216S IECs compared with IFN-γ–treated control cells (Figure 5, G and H, and Supplemental Figure 11). These data indicate that a loss-of-function mutation in TCPTP predisposes to greater tight junction reorganization in response to IFN-γ, and increased permeability, consistent with observations of barrier disruption in TCPTP-deficient mice.

TCPTP suppresses expression of the cation-selective pore, claudin-2, in intestinal epithelium. The "pore pathway" of increased paracellular flux of electrolytes (i.e., Na^+) and water into the intestinal lumen can promote diarrhea and is mediated by select members of the claudin superfamily, most prominently the cation-selective protein, claudin-2 (25, 30, 39–41). We report increased epithelial claudin-2 mRNA in *Tcptp*-HET and -KO mice across intestinal regions (Supplemental Figure 10B). Claudin-2 immunostaining was elevated in the cecum of both HET and KO mice compared with WT (Figure 6A). Localization of claudin-2 was strongest at the crypt base. The ileum, cecum, and proximal and distal

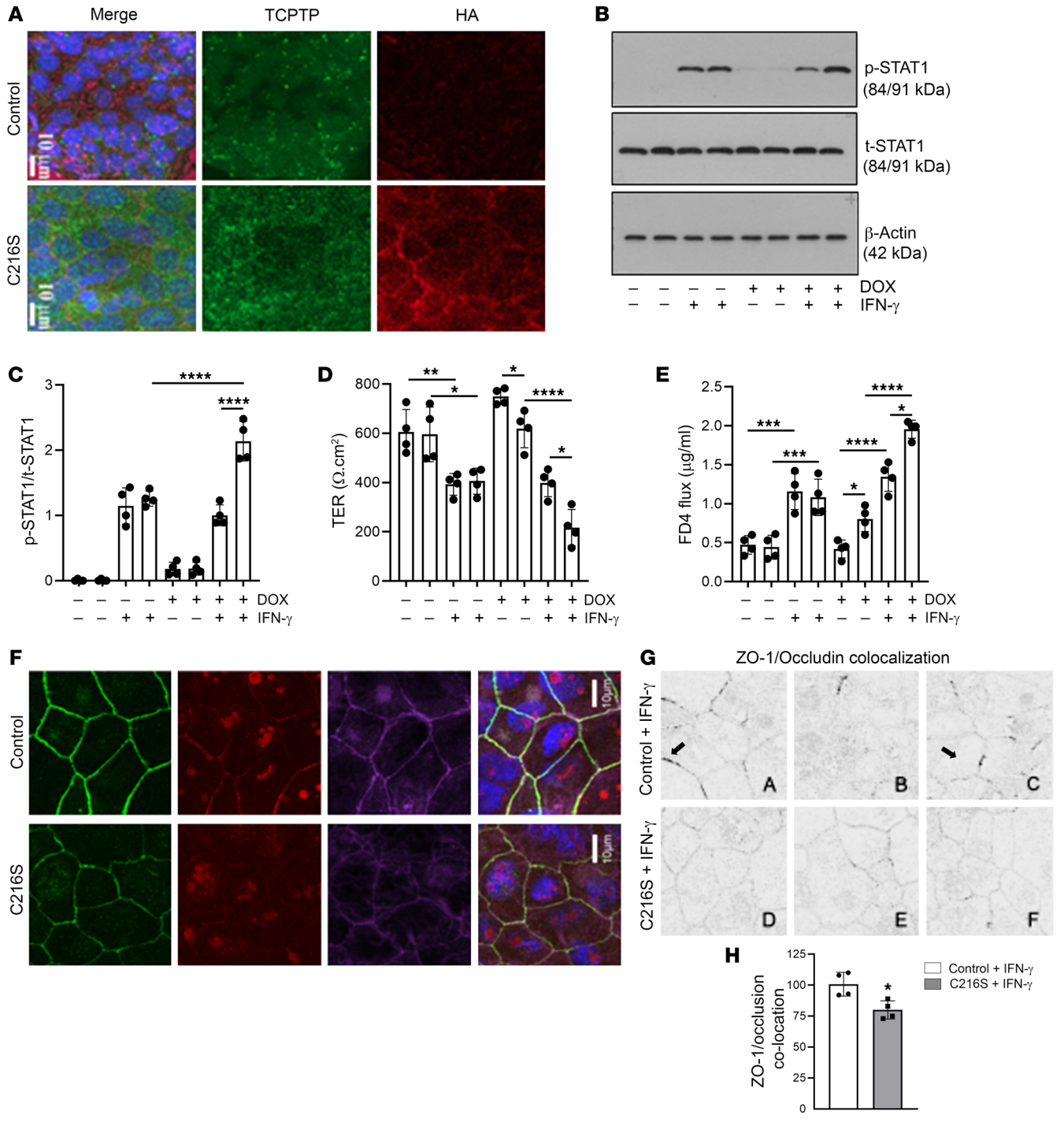

Figure 5. A TCPTP loss-of-function mutation increases cytokine-induced tight junction remodeling. (**A**) Fluorescence micrographs of TCPTP (green) and HA (red) expression in doxycycline-treated (DOX-treated) (15 μg/mL; 48 hours) control and C216S-TC45–transfected HCA-7 IECs (merge image includes DAPI nuclear staining shown in blue). Scale bars: 10 μm. (**B**) Western blots showing STAT1 tyrosine phosphorylation (Y701) after basolateral addition of IFN-γ (200 U/mL, 6 hours) to DOX-pretreated control or C216S-TC45 HCA-7 IECs. Total STAT1 and β-actin levels shown for all conditions. (**C**) STAT1 phosphorylation relative to total STAT1 protein was determined by densitometry. (**D**) Control and C216S HCA-7 cells were cultured on Transwells prior to treatment with vehicle (PBS) or DOX (15 μg/mL; 48 hours) and subsequent treatment with IFN-γ (1000 U/mL, 24 hours). TER was measured and expressed as Ω/cm^2. (**E**) FD4 permeability was calculated after 6 hours of IFN-γ treatment and expressed as mg/mL. (**F**) Representative image showing ZO-1 and occludin localization following IFN-γ treatment of DOX-pretreated control and C216S-TC45 IECs (merge image includes DAPI nuclear staining shown in blue). Scale bars: 10 μm. (**G** and **H**) Color conversion (in Adobe Photoshop) and quantification (ImageJ software, NIH) of ZO-1/Occludin colocalization (black arrows) in DOX-pretreated control (top row) and C216S-TC45 IECs (bottom row) exposed to IFN-γ (200 U/mL, 6 hours). Original magnification, 63×. Data shown as mean ± SD. Statistical significance was calculated by 1-way ANOVA and Student-Newman-Keuls posttest. Comparisons between 2 groups were by 2-tailed Student's *t* test ($n = 4$). $^*P < 0.05$; $^{**}P < 0.01$; $^{***}P < 0.001$; $^{****}P < 0.0001$.

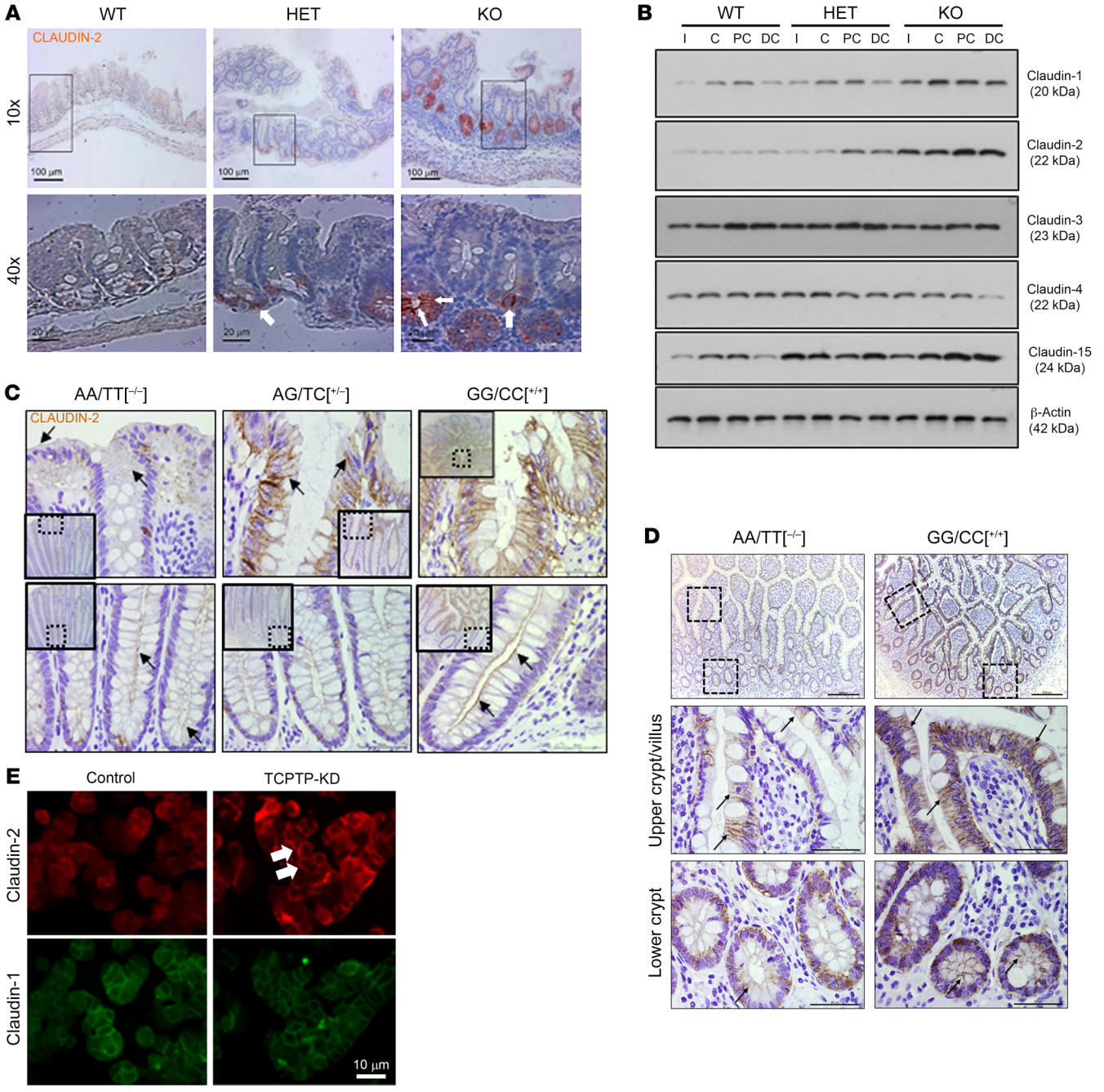

Figure 6. TCPTP deficiency increases intestinal expression of claudin-2 in vitro, in vivo, and in *PTPN2*-genotyped CD patients. (**A**) Representative confocal micrograph showing claudin-2 expression in cecum from *Tcptp* WT, HET, and KO mice. Original magnification: ×10; ×40. (**B**) Expression of TCPTP; claudin-1, -2, -3, -4, and -15; and β-actin in isolated IECs from cecum of *Tcptp* WT and KO mice. The same β-actin blot was used in Figure 3G because blots were generated from the same mouse samples. (**C**) Immunohistochemistry of claudin-2 expression in colonic tissue from CD patients with WT TCPTP who tested negative for the rs1893217 loss-of-function *PTPN2* mutation (AA/TT[−/−]; n = 5), 1 copy of the rs1893217 mutation (GA/CT[+/−]; n = 5), or 2 copies of the mutation (GG/CC[+/+]; n = 2). Arrows indicate membrane localization of claudin-2. Scale bars: 100 μm (original magnification, 20×), insert 50 μm. (**D**) Immunohistochemistry of Claudin-2 expression in ileum from CD patients with WT TCPTP – *PTPN2* rs1893217 SNP null (AA/TT[−/−]; n = 6) – or who tested homozygous for the PTPN2 loss-of-function variant (GG/CC[+/+]; n = 6). Arrows indicate membrane localization of claudin-2. Scale bars: 200 μm, insert 50 μm. (**E**) Representative fluorescence images of claudin-2 and claudin-1 in control-shRNA and TCPTP-shRNA (TCPTP-KD) Caco-2BBe IECs cultured on glass coverslips. Arrows indicate increased claudin-2 membrane localization (n = 3).

colon had increased claudin-2 protein in IECs across all regions in KO versus WT mice, with higher claudin-2 also observed in cecum and distal colon of HET versus WT mice (Figure 6B and Supplemental Figure 12A). Of the barrier-promoting claudins, claudin-1 was increased in the distal colon of KO mice while claudin-3 and -4 were unchanged (Figure 6B and Supplemental Figure 12, B–D). Moreover, an additional cation pore, claudin-15, was increased in the colon of KO mice (Figure 6B and Supplemental Figure 12E).

Table 1. Patient characteristics

Variant	Diagnosis	Region	Sex	Age
AA/TT	CD	Colon	F	47
AA/TT	CD	Colon	M	22
AA/TT	CD	Colon	F	43
AA/TT	CD	Colon	F	73
AA/TT	CD	Colon	F	32
AA/TT	CD	Colon	F	24
GA/CT	CD	Colon	M	74
GA/CT	CD	Colon	F	16
GA/CT	CD	Colon	F	47
GA/CT	CD	Colon	F	45
GA/CT	CD	Colon	F	70
GG/CC	CD	Colon	M	34
AA/TT	CD	Ileum	F	47
AA/TT	CD	Ileum	M	22
AA/TT	CD	Ileum	F	43
AA/TT	CD	Ileum	F	73
AA/TT	CD	Ileum	F	32
AA/TT	CD	Ileum	F	24
GG/CC	CD	Ileum	F	46
GG/CC	CD	Ileum	M	25
GG/CC	CD	Ileum	F	36
GG/CC	CD	Ileum	M	28
GG/CC	CD	Ileum	F	38
GG/CC	CD	Ileum	M	41

The physiological relevance of increased claudin-2 expression in *Tcptp*-HET and -KO mice was demonstrated in colonic tissues from CD patients harboring the loss-of-function IBD-associated *PTPN2* rs1893217 SNP (Table 1). Patients homozygous (GG/CC) or heterozygous (GA/CT) for this SNP displayed increased claudin-2 expression in colonic and ileal (Figure 6, C and D, and Supplemental Figure 13A) epithelium compared with patients with WT *PTPN2* alleles (AA/TT). Using stable PTPN2-knockdown (PTPN2-KD) Caco-2BBe IECs, we also confirmed increased claudin-2 immunofluorescence staining at cell membranes compared with control cells while claudin-1 was unchanged (Figure 6E). Claudin-2 KD by siRNA (Supplemental Figure 13, B–D) rescued TER in TCPTP-KD epithelial monolayers but had no effect on the elevated FD4 permeability (Figure 7, A and B), thus demonstrating that claudin-2 mediates the TER defect in TCPTP-deficient IECs. There are conflicting reports of the effect on tight junction architecture in transfected claudin-2–overexpressing cells (40, 42). Freeze fracture electron microscopy indicated that TCPTP-KD IECs did not display any gross alterations in tight junction network morphology (Figure 7C). The number of strand discontinuities in the P-face strands was slightly increased in TCPTP-KD (5.8 breaks/μm) compared with WT Caco-2BBe cells (3.6 breaks/μm), and similar increases in discontinuities have been observed when the cis interface of claudin-15 was mutated (43). These data suggest that partial TCPTP loss modulates tight junction composition rather than disrupting overall tight junction strand integrity.

TCPTP limits claudin-2 by restricting STAT1-mediated transcription of claudin-2 and hepatocyte growth factor activator inhibitor-1, a suppressor of the integral membrane serine protease, matriptase. In addition to the transcriptional control of CLDN2, claudin-2 levels at the tight junction are also modulated by the serine protease matriptase (*ST14*; ref. 44). We found that TCPTP loss modulated this mode of claudin-2 regulation since matriptase mRNA and protein levels were significantly reduced in colonic tissue from *Tcptp*-KO mice compared with WT mice (Figure 8A and Supplemental Figure 14A). Moreover, IFN-γ treatment of C216S-TC45–expressing IECs significantly reduced matriptase expression and concomitantly increased membrane claudin-2 (Figure 8B). TCPTP-KD IECs (Supplemental Figure 14B) were more susceptible to IFN-γ induction of claudin-2 expression, and we demonstrated that IFN-γ selectively reduced matriptase protein and mRNA levels in TCPTP-deficient but not control IECs (Figure 8C and Supplemental Figure 15). To further elucidate the mechanism of TCPTP regulation of matriptase and claudin-2, we performed siRNA knockdown of STAT1 or HAI-1/*SPINT1*, which acts as a physiological inhibitor and regulator of matriptase activity and expression (45). Knockdown of STAT1 or HAI-1 normalized claudin-2 expression, and reversed matriptase suppression, in TCPTP-KD (shRNA) Caco-2 IECs, following IFN-γ challenge (Figure 8C and Supplemental Figure 15). Thus, TCPTP limits claudin-2 levels by (a) inhibiting STAT1-mediated transcription of (a) claudin-2 and (b) HAI-1, as well as (c) inhibiting STAT-induced, HAI-1-mediated suppression of matriptase (*ST14*) transcription.

Recombinant matriptase rescues TER and normalizes claudin-2 expression in TCPTP-deficient IECs. To confirm a functional role for matriptase loss in the TER barrier defect observed in TCPTP-KD IECs, we performed rescue experiments where TCPTP-stable SD HT-29 IECs were treated with recombinant human matriptase (rMAT). Basolateral, but not apical, application of rMAT to TCPTP-KD monolayers significantly increased TER over 24 hours, indicating rescue of baseline TER (Figure 8D). Elevated claudin-2 in TCPTP-KD cells was reversed by basolateral addition of rMAT, indicating that rMAT rescued the decreased TER in TCPTP-deficient IEC by reducing claudin-2 (Figure 8, E and F). Recombinant matriptase had no effect on TCPTP levels in control or KD cells (Supplemental Figure 14C). This demonstrates that TCPTP suppresses claudin-2 levels by restricting cytokine-induced repression of matriptase expression in IECs, thus preserving a key regulatory signaling pathway to control claudin-2. Moreover, the decrease in TER due to loss of TCPTP activity is mediated by elevated claudin-2, and this defect can be rescued by recombinant matriptase.

Discussion

One of the initial and fundamental disturbances in intestinal homeostasis that contributes to IBD pathogenesis is increased intestinal permeability, which occurs primarily through disruption of cellular tight junction composition (6, 11). An altered complement of claudin family members — such as increased claudin-2 in inflammatory states — increases charge-selective paracellular electrolyte permeability via the "pore" pathway. The "leak" pathway, which facilitates increased paracellular permeability to macromolecules and non–charge-selective passage of electrolytes, is increased by removal of proteins such as occludin and ZO-1 from the tight junction. An "unrestricted" mode of permeability, which displays neither charge nor size selectivity, can also occur

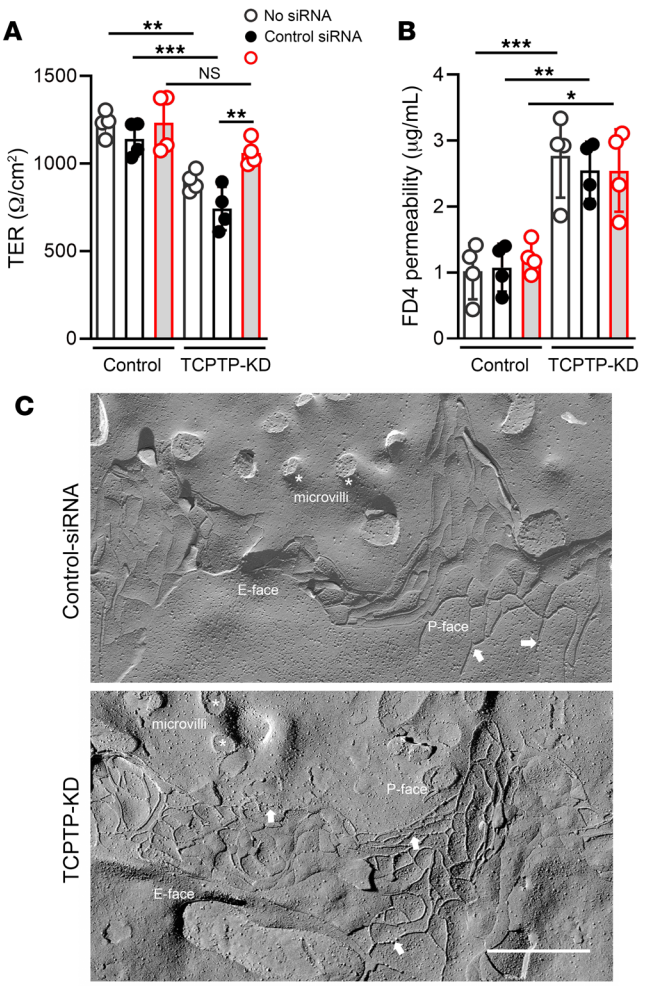

Figure 7. Claudin-2 mediates altered TER but not FD4 permeability in TCPTP-deficient epithelial cells. Control-shRNA and TCPTP-KD Caco-2BBe IECs cultured on Transwells for 7 days prior to treatment for 48 hours with no siRNA (open black circle) or control/scrambled (filled black circle) or CLDN2 (open red circle) siRNA. (**A**) TER and (**B**) FD4 permeability was measured (n = 4). (**C**) Tight junction freeze fracture morphology of control-shRNA (top) and TCPTP-KD (bottom) Caco-2BBe cells. The overall morphology of both the control and PTPN2-KD cells appeared similar in both the control and TCPTP-KD cells. Comparable fracture planes show continuous strands consistently segregating to the protoplasmic (P-) face (indicated with arrows) and grooves left in the exoplasmic (E-) face. However, more discontinuities in the P-face strands were observed in TCPTP-KD cells. Microvilli indicated by asterisks. Scale bar: 500 nm. Data are expressed as mean ± SD (n = 4). Comparisons between multiple groups were by 1-way ANOVA and Tukey's posttest. *P < 0.05; **P < 0.01; ***P < 0.001.

due to IEC apoptosis or increased cell shedding (4, 7, 12, 46, 47). While unrestricted permeability — assessed by RD70 flux — was not increased in *Tcptp*-deficient mice, we did observe both forms of tight junction–mediated defect (pore and leak). Intriguingly, different intestinal regions revealed distinct patterns of barrier defect, with the cecum exhibiting a titrated increase in macromolecule permeability and reduced TER based on *Ptpn2/Tcptp* genotype. This aligns with described differences in TER in midcolonic versus distal colonic tissues from control mice (48). In addition to the tight junction–regulated paracellular route, transcellular routes of solute passage across the gut epithelium have also been identified, including endocytosis, antigen transcytosis by Peyer patch M cells, and goblet cell–associated antigen passages (GAPs; ref. 49). While small intestinal GAPs could contribute to FD4 permeability in *Tcptp*-KO mice, it is notable that they are actually reduced during inflammation (50).

While expression of inflammatory cytokines varied across intestinal regions, IFN-γ was consistently elevated in *Tcptp*-HET and -KO mice in all large intestinal regions examined. In addition, increased crypt depth, possibly indicating increased epithelial proliferation, was apparent in the cecum and proximal colon but not the distal colon of KO mice. Factors responsible for these segmental variations may include altered signaling between IECs and a variety of mucosal immune cells, as well as disruption of homeostatic host-commensal microbe interactions with the epithelium. The observed regional variations in cytokine production were associated with altered relative abundance of cytokine-producing T cell subsets in *Tcptp*-deficient mice (51). Increased IFN-γ$^+$ T cell abundance and serum IFN-γ was consistent with previous studies of these mice, and CD4-specific deletion of TCPTP (24, 32, 52). While these mice showed increased IL-17$^+$CD4$^+$ T cells and Tregs, we observed decreased IL-17$^+$CD4$^+$ T cells, and no change in overall Treg abundance, but reduced IL-10$^+$ Tregs in KO mice (Supplemental Figure 5G). Of note, thymic Tregs were increased in whole-body *Tcptp*-KO mice on the C57BL/6 background, while in an arthritis mouse model, TCPTP haploinsufficiency facilitated IL-6–driven Treg dedifferentiation (loss of FoxP3) and conversion to IL-17$^+$ exTregs that were associated with subclinical colonic inflammation (53, 54). This suggests a critical role for TCPTP at the intersection of intestinal and joint inflammation (55). Moreover, the shared association of PTPN2 mutations and intestinal permeability with several chronic diseases may indicate potential broad mechanistic overlap (7, 19). In addition, our current data showing that KO mice exhibited increased abundance of M1-like "inflammatory" macrophages support our recent findings that TCPTP controls bidirectional macrophage-epithelial cell communication to restrict epithelial tight junction permeability and M1-like polarization (21).

While TCPTP deficiency has effects on immune cells, our in vitro and *Ptpn2*$^{\Delta IEC}$ mouse data now show that TCPTP also has critical epithelial cell–intrinsic functions. Intestinal tissues from these mice showed no increase in in vivo FD4 permeability, but displayed region-specific increases in FD4 flux and reduced TER, consistent with underlying permeability defects. This region-specific pattern was also evident following in vivo challenge with inflammatory cytokines that we identified were elevated in whole-body *Tcptp*-KO mice. Overall, these data confirm that loss of TCPTP expression in IECs alone is sufficient to compromise intestinal permeability in a region-specific manner and also to increase susceptibility to barrier-altering inflammatory cytokines.

Our data indicate that the increase in FD4 permeability in *Tcptp*-deficient mice is likely due to remodeling of apical tight junctions, arising directly from reduced TCPTP in IECs and indirectly through increased inflammatory cytokines. Indeed, KO mice exhibited clear disruption of occludin and ZO-1 localization in intestinal epithelium, while IECs expressing C216S showed a

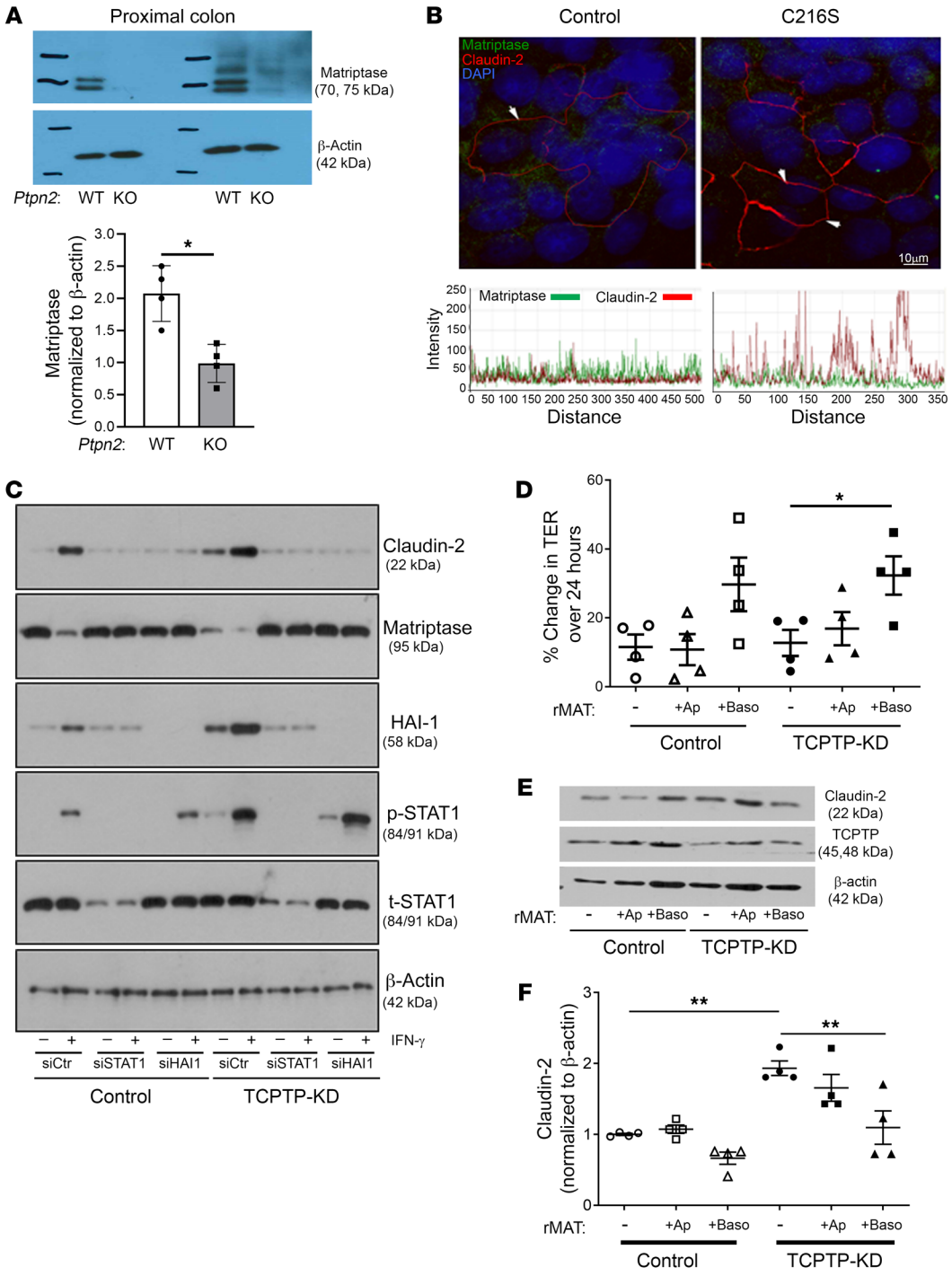

Figure 8. TCPTP promotes matriptase regulation of claudin-2, and recombinant matriptase rescues the claudin-2–mediated barrier defect in TCPTP-deficient IECs. (**A**) Western blot of matriptase and β-actin in proximal colon (whole tissue) from *Tcptp* WT and KO mice. Densitometric quantification of Western blot colonic whole tissue matriptase expression normalized to tissue β-actin (*$P < 0.05$ vs. WT; $n = 4$). (**B**) Fluorescence micrograph showing line scan analysis of fluorescence intensity of claudin-2 (red; white arrows) and matriptase (green) expression in IFN-γ–treated (200 U/mL, 48 hours) control-shRNA and C216S-TC45 HCA-7 IECs. Representative of 4 to 6 scans per treatment condition ($n = 4$). (**C**) Western blots of control-shRNA and TCPTP-KD Caco-2 IECs transfected with control/scrambled siRNA (siCtr), or siRNA targeting STAT1 or hepatocyte growth factor activator inhibitor-1 (HAI-1), and probed for claudin-2, matriptase, HAI-1, phosphorylated (Y701) and total STAT1, and β-actin (**D**) TCPTP-shRNA– (TCPTP-KD) or control-shRNA–transfected HT-29 IEC monolayers grown on Transwells were treated apically or basolaterally with recombinant human matriptase (rMAT; 5 nM), and TER change after 24 hours was measured and compared with unchallenged monolayers (–). (**E**) Expression of claudin-2 in control-shRNA and TCPTP-KD HT-29 monolayers was determined by Western blotting and (**F**) quantified by densitometry. Data expressed as mean ± SD. Comparisons between multiple groups were by 1-way ANOVA and Student-Newman-Keuls posttest ($n = 4$). Comparison between 2 groups was by 2-tailed Student's *t* test. *$P < 0.05$; **$P < 0.01$.

significant loss ($P < 0.05$) of occludin and ZO-1 membrane colocalization following IFN-γ challenge. Induction of TC45-C216S by itself was sufficient to reduce TER and increase FD4 flux and exacerbate IFN-γ's effects on both parameters. While IFN-γ disrupted ZO-1 colocalization with occludin and claudin-4, membrane ZO-1 was not disrupted in non–cytokine-treated C216S cells, suggesting that the functional defects in untreated cells cannot be attributed to ZO-1 mislocalization. The C216 site is a highly conserved and critical part of the protein tyrosine phosphatase catalytic region (38). Of clinical relevance, a loss-of-function mutation of the C216 site (C216G) is a monogenic driver of autoimmune enteropathy, thus emphasizing the disease-causing potential of deficient PTPN2 activity (38). Mechanistically, removal of ZO-1 and occludin can occur by endocytic processes in response to MLC phosphorylation, which was also elevated in *Tcptp*-KO, and to a lesser extent in *Tcptp*-HET, mice. MLC phosphorylation is a point of convergence for both IFN-γ–Rho kinase–mediated tight junction protein internalization as well as TNF-α–MLC kinase–mediated epithelial permeability, and its increase is consistent with the elevated IFN-γ and TNF-α levels we detected in TCPTP-deficient mouse intestine (33, 56).

The claudin family of tetraspanning membrane proteins is essential for homeostatic electrolyte flux, fluid uptake, and sodium recycling in electrolyte-coupled nutrient absorption (41, 57–59). Increased epithelial expression of the cation pore-forming molecule claudin-2 is a feature of IBD but can also have protective roles against pathogen infection (39, 46). Claudin-2 shows a region-specific distribution pattern in the intestine with higher expression in leaky epithelia of the small intestine and lower levels in tight epithelia of the large intestine (60, 61). Thus, elevated claudin-2 expression in the large intestine is of functionally greater significance than in a leakier epithelium, as it facilitates fluid loss consistent with IBD-associated diarrhea (39, 40, 62). Here, we observed increased claudin-2 expression in large intestine from *Tcptp*-HET and -KO mice. This is consistent with the elevated levels of IL-6 in all regions and IL-22 in the distal colon of *Tcptp*-deficient mice, because both of these cytokines are known inducers of claudin-2 expression (Supplemental Figure 2 and refs. 46, 63). We previously identified that IFN-γ induces claudin-2 expression in TCPTP-deficient IECs by STAT1 activation and binding to STAT-binding motifs in the *CLDN2* promoter (30). This was supported by data from *Ptpn2*$^{\Delta IEC}$ mice confirming increased baseline claudin-2 expression, and phosphorylation of STAT1 and STAT3 that was accentuated by in vivo IL-6 or IFN-γ administration, while claudin-2 was also increased in CD patients with the *PTPN2* rs1893217 SNP. Of note, the cation pore, claudin-15, was also increased in colonic epithelial cells in whole-body *Tcptp*-KO mice, thus potentially offering an additional route for paracellular Na^+ flux.

Our present findings indicate that TCPTP is a positive regulator of the serine metalloproteinase matriptase (*ST14*). Matriptase regulates epithelial barrier integrity by promoting the removal of claudin-2 from the tight junction, leading to its subsequent proteasomal degradation (44, 64). In IECs expressing the TCPTP loss-of-function mutant, we observed a reversal of the normal homeostatic equilibrium between high matriptase and low claudin-2 seen in control IECs. IFN-γ significantly reduced matriptase expression in C216S-TC45 IECs while increasing membrane claudin-2 levels (Figure 8B). We found that TCPTP restricted the capacity of IFN-γ to reduce matriptase mRNA levels through STAT1-dependent induction of the matriptase inhibitor, HAI-1, and that claudin-2 functionally mediated the reduced TER in TCPTP-deficient IECs. Rescue of TER in PTPN2-KD IECs with recombinant matriptase supports previous findings of matriptase as a negative regulator of claudin-2 but also reveals that matriptase signaling can be targeted to correct elevated claudin-2 arising from reduced TCPTP activity.

In summary, we show that TCPTP protects the intestinal epithelial barrier by restricting cytokine-induced tight junction remodeling and increased permeability to macromolecules. In addition, TCPTP exerts bimodal inhibition of the cation pore-forming molecule claudin-2 to restrict paracellular flux of sodium and water. These findings identify mechanisms by which insufficient TCPTP expression, and/or loss-of-function mutations in the *PTPN2* gene, can contribute to elevated intestinal permeability that is a feature of chronic intestinal inflammatory diseases and plays a critical role in their onset.

Methods

Macroscopic assessment of constitutive Tcptp-deficient mice. *Tcptp* WT and constitutive, whole-body heterozygous (HET) and knockout (KO) BALB/c mouse littermates (age matched at 17–24 days old) of both sexes were weighed (31, 32). Spleen weight, colon length, and colon wet weight were also measured.

Generation of inducible Ptpn2$^{\Delta IEC}$ *KO mice*. *Ptpn2*$^{tm1a(EUCOMM)Wtsi}$/Wtsi mice (obtained from Wellcome Trust) have exon 3 of the *Ptpn2* gene flanked by *loxP* sites and a *neoR-lacZ* cassette flanked by FRT sites in intron 2 (Supplemental Figure 7A). To generate mice with inducible deletion of *Ptpn2* in IECs, we crossed these mice with *Vil-Cre/ERT2* mice [B6.Cg-Tg(Vil1-cre/ERT2)23Syr/J] (provided by Sylvie Robine, Institut Curie, Paris, France) that carry a tamoxifen-inducible *ERT2* gene under the control of the *Villin* promoter (65). The resulting double-heterozygous mice were crossed with transgenic mice expressing FLP recombinase in the germline [B6.129S4-*Gt(ROSA)26Sor*$^{tm1(FLP1)Dym}$/RainJ; The Jackson Laboratory] to remove the *neoR-lacZ* cassette. Mice were backcrossed to a C57BL/6J background for 10 generations and made homozygous for *Ptpn2*$^{loxP/loxP}$ without or with hemizygous *Vil-Cre/ERT2* and maintained in that state. Cre-mediated recombination was induced by i.p. injection in 6- to 10-week-old mice of 1 mg TMX (50 mg/kg body weight; T5648, MilliporeSigma), dissolved in sterile corn oil (C8267, MilliporeSigma), for 5 consecutive days. Tissues were harvested 4 weeks after the final administration of TMX.

In vivo cytokine administration. For in vivo cytokine administration, 6- to 8-week-old *Ptpn2*-Villin-Cre/ERT2$^{fl/fl}$ and *Ptpn2*$^{fl/fl}$ littermates were injected with TMX on 5 consecutive days (as above). Four weeks later, the mice were injected once with IL-6 (100 ng), IFN-γ (1000 U) or TNF-α (100 ng), or IFN-γ and TNF-α in combination and intestinal tissues harvested 24 hours later for Ussing chamber (Physiological Instruments) measurements.

Mouse barrier function studies. *Tcptp* wild-type (WT), heterozygous (HET), and constitutive knockout (KO) Balb/c mice (littermates, age matched within genotypes; males and females, 17–21 days old) were housed under conventional housing conditions. In vivo permeability of FD4 (MilliporeSigma; catalog 46944; hydrodynamic diameter, 28 Å; 80 mg/mL) and RD70 (MilliporeSigma; catalog R9379; 20 mg/mL) was determined following oral gavage (100 μL volume).

After 5 hours, serum was harvested retro-orbitally. Fluorescence of fluorescein and rhodamine in samples loaded into a black plate was measured using excitation wavelengths of 495 nm and 555 nm, and emission wavelengths of 525 nm and 585 nm, respectively, using a SpectraMax iD3 plate reader (Molecular Devices), aligned with established protocols (46).

For ex vivo permeability studies, mice were sacrificed by cervical dislocation, and full-thickness segments of jejunum, distal ileum, cecum, proximal colon, and distal colon were mounted in Ussing chambers. Tissues were bathed bilaterally with Ringer's physiological solution (composition in mM: 140 Na^+, 5.2 K^+, 1.2 Ca^{2+}, 0.8 Mg^{2+}, 120 Cl^-, 25 HCO_3^-, 2.4 $H_2PO_4^-$, 0.4 HPO_4^{2-}, and 10 glucose) with 10 mM mannitol substituted for glucose in apical bathing media for small intestinal tissues to prevent activation of Na^+-glucose cotransport. A transepithelial current pulse of 10 μA was administered to assess tissue viability, and TER was calculated using Ohm's law (66). To test for permeability, FD4 was added to the mucosal medium at a final concentration of 1 mg/mL. Serosal samples were collected at *t*0 and after 2 hours (*t*120) and calculated for change in concentration relative to the initial FD4 concentration in mucosal samples (*t*0). Fluorescence was analyzed with a SpectraMax iD3 microplate reader. Tissue viability at the end of the experiment was confirmed by challenge with the cAMP agonist forskolin (20 μM, bilaterally) and the Ca^{2+} agonist carbachol (300 μM, serosally). Electrogenic ion transport responses were measured and expressed as the change in short-circuit current (ΔI_{SC}), in μA/cm².

Histology and immunohistochemistry of mouse tissue. Intestinal segments (distal ileum, cecum, proximal and distal colon) from WT, HET, and KO mice (as above) were fixed in 4% paraformaldehyde (PFA) and exposed to a graded ethanol series before embedding in paraffin. Tissue blocks were cut into 5 μm sections, deparaffinized, and rehydrated in a descending ethanol series. Intestinal cross-sections were used for morphometric measurements. Only well oriented sections with bottom-to-top crypt-villus axis visibility were used in the analysis. The straight line tool from FIJI software was calibrated using the scale bar from the image being measured. A straight line was drawn measuring crypt depth, villus length, and crypt width. All data for each parameter being measured were averaged per mouse with a minimum of 4 measurements for each parameter per mouse. For cell counting, total number of IECs per crypt was counted using the Cell Counter tool in FIJI software. Immunostaining of sections for phosphorylated STAT1 (Tyr701) and phosphorylated MLC (Cell Signaling Technology; catalog 9167 and catalog 3671, respectively) was performed by standard immunohistochemistry with secondary Alexa Fluor 488 goat anti-rabbit (Invitrogen, Thermo Fisher Scientific, catalog A-11008). Occludin and ZO-1 staining was performed using a 550 MaxFluor mouse on mouse kit (MaxVision Biosciences Inc.; catalog MF02-M). Colonic tissue was stained with anti-St14 (Biovision; catalog 3855-100) and a MaxFluor 488 rabbit on mouse kit (MaxVision Biosciences Inc.; catalog MSAB21-M). Claudin-2 was detected using primary and secondary (anti-rabbit) antibodies from Invitrogen, Thermo Fisher Scientific (catalog 32-5600), and Cell Signaling Technology (catalog 7074), respectively. Assessment of mouse claudin-2 by bright-field imaging was conducted at the UCSD histology core facility.

Confocal microscopy and localization studies. A Zeiss LSM 510 confocal microscope was used to acquire images of immunostained cells. Leica SP5 and inverted Zeiss 880s microscopes were used to image mouse intestinal segments. Image processing for line scans was performed using the LSM 510 colocalization software. Pseudo-color yellow colocalization was inverted to black, and all other colors were suppressed as white using Adobe Photoshop; the resulting density was quantified using ImageJ. Mouse tissue sections were imaged using the Leica SP5 with resonance settings. All mouse and cell line confocal immunofluorescence microscopy was conducted at the University of California, Riverside (UCR), or UCSD microscopy core facilities.

Immunohistochemistry of human intestinal sections. Human samples were obtained from patients with IBD attending the IBD Center at Cedars-Sinai Medical Center after informed consent was received. Samples with active inflammation were excluded following pathologist review. Diagnoses of IBD were made using standard clinical, endoscopic, radiological, and histological criteria. Genotyping and quality control for the rs1893217 SNP were performed as previously described utilizing the Immunochip (Illumina) platform (67). Formalin-fixed, paraffin- embedded human colon and ileal tissues were sectioned at 5 μm and processed for immunohistochemistry as follows: after deparaffinizing, antigen epitopes were retrieved in 10 mM sodium citrate buffer pH 6.0 (20 minutes at ~96°C). Endogenous peroxide was quenched with 3% hydrogen peroxide. Nonspecific antigens were blocked with blocking buffer (2% normal donkey serum [NDS], 1% albumin, 0.1% Triton X-100, 0.05% Tween 20, and 0.05% sodium azide in PBS) for 30 minutes at room temperature. The biotinylated primary antibody (Claudin-2; Abcam; catalog ab53032; 1:400 in PBS, 5% NDS) was applied for 1 hour at room temperature. Detection was performed by incubation with streptavidin-coupled HRP (N100, Thermo Fisher Scientific) for 1 hour and subsequent addition of DAB substrate according to the manufacturer's protocol (Cell Signaling Technology, catalog 8059). Slides were mounted with Permount mounting medium (Thermo Fisher Scientific) and visualized with a Leica DM5500B microscope with DFC450 C camera. All confocal immunofluorescence microscopy was conducted at the UCR or UCSD microscopy core facilities.

Tissue cytokine analysis. For cytokine protein detection, Luminex inflammatory cytokine kits (Affymetrix) were processed according to manufacturer's instructions and quantified on Luminex MagPix (Luminex Corp.). *Il13* mRNA expression was determined by reverse transcription PCR.

Tissue RNA isolation and quantitative PCR. Total RNA was extracted from intestinal segments from mice using TRIzol reagent according to the manufacturer's instructions (Invitrogen, Thermo Fisher Scientific). RNA purity and concentration were assessed by absorbance at 260 and 280 nm. One microgram of total RNA was transcribed into cDNA using qScript cDNA SuperMix (Quanta Biosciences). Two microliters of 5×-diluted cDNA was amplified using gene-specific primers and GoTaq Green, 2× mix (Promega; sequences listed in Supplemental Table 1). Gene-specific primers were used with the following conditions: initial denaturation 95°C for 5 minutes, followed by 30 cycles 95°C for 30 seconds (denaturation), 55°C for 30 seconds (annealing), and 72°C for 30 seconds (extension). The final extension was 72°C for 5 minutes. Mouse GAPDH was used as an endogenous control.

Flow cytometry. Lamina propria immune cells were isolated as described (68). For analysis of myeloid immune cells, the cells were washed in PBS; incubated with FcR blocking antibody (130-092-575, Miltenyi Biotec) for 10 minutes; and stained with Pacific Blue anti–mouse CD45 (clone 30-F11, catalog 103125), Brilliant Violet 650 (BV650) anti-CD3 (clone 17A2, catalog 100229), anti-NK1.1–BV650

(clone PK136, catalog 108735), anti-B220–BV650 (clone RA3-6B2, catalog 103209), anti-CD11b–BV605 (clone M1/70, catalog 101237), anti-CD11c-PECy7 (clone N418, catalog 117338), PerCPCy5.5 anti-mouse anti-Ly6C (clone HK1.4, catalog 128011), APC anti-mouse anti-F4/80 (clone BM8, catalog 123115), and anti–mouse CD64-PE (clone X54-5/7.1, catalog 139303), all from BioLegend, and Alexa Fluor 700 anti–mouse MHC-II (clone M5/114.15.2, catalog 56-5321-80, Thermo Fisher Scientific), for 15–30 minutes. Zombie NIR live dead stain (BioLegend) was used for discrimination between live and dead cells. For cytokine staining, the cells were incubated with ionomycin and PMA in the presence of Brefeldin A (eBioscience, Thermo Fisher Scientific) for 3.5 hours prior to surface staining with anti–CD25–Alexa Fluor 700 (clone PC61, catalog 102024), anti–CD3-PerCPCy5.5 (clone 17A2, catalog 100217), anti–CD4-BV510 (clone GK1.5, catalog 100449), and anti–CD8-BV570 (clone 53-6.7, catalog 100739), all from BioLegend, for 15 minutes. Cells were then fixed with the FoxP3 staining kit (catalog 00-5523-00, eBioscience, Thermo Fisher Scientific) according to the manufacturer's instruction; stained with anti-FoxP3–Pacific Blue (clone MF-14, catalog 126409, BioLegend), anti–IFN-γ–PECy7 (clone XMG1.2, catalog 505825), anti–IL-17–APC (clone TC11-18H10.1, catalog 506915), anti–TNF-α–BV650 (clone MP6-XT22, catalog 506333), and anti–IL-22–PE (clone Poly5164, catalog 516404) for 30 minutes; and washed in PermWash buffer (catalog 554723, BD). Samples were acquired on an LSRII cytometer (BD) and analyzed using FlowJo (Tree Star, Inc.).

Lentiviral vectors. A vector containing the predominant 45 kDa splice variant of TCPTP (EGFP-C1-TC45) was provided by Tony Tiganis (Monash University, Melbourne, Victoria, Australia). pCMV-HA construct and Lenti-X Tet-On Advanced Vector Set (Clontech) and doxycycline (MilliporeSigma) were obtained from the suppliers listed. All other reagents were of analytical grade and acquired commercially. EGFP-TC45 constructs were used to form the C216S mutant (site-directed mutagenesis kit, Clontech). Resulting constructs were subcloned into pCMV-HA (Clontech) to obtain the HA tag. PCR was used to add compatible restriction enzyme sites, Bam-HI and MluI, to the HA-TC45 constructs (C216S). These inserts were subcloned into the lentiviral vector pLVX-Tight-Puro. The lentiviral HA-C216S and empty vector control constructs were transfected into a packaging cell line (HEK293T; experiment performed at UCSD) to produce lentivirus. HCA7 human epithelial cells were infected with the lentiviral constructs, to generate a cell line stably expressing TC45-C216S.

TCPTP mutant–expressing IECs. The human colonic epithelial cell line, HCA7 (obtained from the late Martin F. Kagnoff, UCSD), transfected with dominant-negative TC45 (C216S), was cultured in a humidified atmosphere with 5% CO_2 in Dulbecco's modified Eagle's/F-12 medium (Mediatech, Inc.) supplemented with 5% Tet-approved newborn calf serum (Clontech) in 75 cm^2 flasks and grown in selection media supplemented with G418 and puromycin per Clontech protocol. Culture medium was changed twice a week. Cells were separated by trypsinization and 0.5×10^6 cells were seeded onto 12 mm Millicell-HA semipermeable filter supports (pore size 0.45 μM) with a surface area of 0.6 cm^2 (MilliporeSigma). The cell monolayers were incubated for 48 hours with media (vehicle) or doxycycline (15 μg/mL) followed by coincubation for 6 or 72 hours with doxycycline (15 μg/mL; apically) and IFN-γ (200 or 500 U/mL; 6 or 24 hours; basolaterally).

In vitro rescue experiments with recombinant matriptase. HT-29 control-shRNA (obtained in-house) and TCPTP-KD cells were seeded on 12-well Transwells (0.5×10^5 cells; ref. 30). On day 5, media were changed, cells were treated with rMAT in serum-free media either apically or basolaterally (5 nM), and TER was measured. The percentage change in TER after 24 hours was calculated from the TER at 0 hours of untreated cells (control and KD, respectively).

Western blot analysis of whole-tissue lysates, isolated IECs, and cell cultures. Isolated whole intestinal tissues were everted and incubated in Cell Recovery Solution (354253, Corning) on ice for 2 hours, then vigorously shaken by hand to release IECs. IECs were washed twice with ice-cold PBS, then lysed with radioimmunoprecipitation assay (RIPA) buffer (50 mM Tris-HCl pH 7.4, 150 mM NaCl, 1% NP-40, 0.5% sodium deoxycholate, and 0.1% SDS) supplemented with 1× protease inhibitor (Roche), 2 mM sodium fluoride, 1 mM PMSF, and phosphatase inhibitors (2 mM sodium orthovanadate, Phosphatase Inhibitor Cocktail 2 and 3, MilliporeSigma) for at least 10 minutes on ice. Cells were homogenized on ice using the Q125 Sonicator (QSonica Sonicators), lysates centrifuged at 16,200*g* at 4°C for 10 minutes, and supernatants collected into new microcentrifuge tubes. Protein concentration was determined using the Pierce BCA Protein Assay Kit (Thermo Fisher Scientific). Loading samples were prepared by mixing the same amount of total protein from each sample with Laemmli loading buffer (60 mM Tris-HCl pH 6.8, 2% SDS, 5% β-mercaptoethanol, 0.01% bromophenol blue, and 10% glycerol), then boiling the samples at 95°C for 10 minutes.

IEC monolayers were removed from insert membranes, suspended in ice-cold RIPA lysis buffer (50 mM Tris, 150 mM NaCl, 0.1% SDS, 0.5% sodium deoxycholate, 20 μM NaF, 1 mM EDTA, 1 μg/mL antipain, 1 μg/mL pepstatin, 1 μg/mL leupeptin, 1 mM $NaVO_3$, 100 μg/mL PMSF), vortexed thoroughly, and subjected to lysis. Lysates were centrifuged at 12,000*g* for 10 minutes at 4°C to remove insoluble material, and protein content was determined as above. Samples were resuspended in loading buffer (50 mM Tris at pH 6.8, 2% SDS, 100 mM dithiothreitol, 0.2% bromophenol blue, 20% glycerol) and boiled for 5 minutes. Equal protein amounts were separated on 4% to 15% polyacrylamide gradient gels to resolve proteins (Mini-protean, Bio-Rad) and transferred onto polyvinylidene difluoride membranes (DuPont-New England Nuclear). Membranes were blocked with a 1% BSA solution in 0.1% Tween/Tris buffer for 30 minutes, followed by incubation with a 0.1% BSA/Tris buffer solution containing primary antibodies at 1:1000 overnight at 4°C. This was followed by three 15-minute washes with wash buffer (0.1% Tween 20, in Tris buffer). After washing, secondary antibody HRP-conjugated goat anti-mouse (catalog 115-036-062) or goat anti-rabbit IgG (111-036-045; both Jackson ImmunoResearch), at 1:1000 dilution in wash buffer, was added for 60 minutes followed by washing (×3). The membrane was treated with chemiluminescence solution per manufacturer's directions (ECL, Pierce, Thermo Fisher Scientific) and exposed to radiographic film (LabScientific). Densitometric analysis was performed using ImageJ. Primary antibodies used for Western blot analysis were mouse monoclonal anti-TCPTP antibody CF-4 (catalog PH03L; Calbiochem, Merck), rabbit anti-TCPTP (catalog 58935), anti–phospho-STAT1 (Tyr701; catalog 9167), anti-STAT1 (catalog 9175), anti–phospho-STAT3 (Tyr705; catalog 9145), anti-STAT3 (catalog 9139), anti–phospho-MLC (Ser19, myosin light chain 2; catalog 3671), and anti-MLC (catalog 3672) (Cell Signaling Technology); rabbit anti-CLDN1 (catalog 51-9000), anti-CLDN2 (catalog 32-5600), anti-CLDN3 (catalog 34-1700), anti-CLDN4 (catalog 32-9400), anti-CLDN15 (catalog 32-9800),

and mouse anti-HA (catalog 26183) (Thermo Fisher Scientific); and rabbit anti-ST14/matriptase (catalog ab28266) and HAI-1 (catalog ab228661) (Abcam); and mouse monoclonal anti–β-actin (catalog number A5316; MilliporeSigma).

In vitro TCPTP KD and quantitative PCR. TCPTP-KD studies were performed in HCA-7 cells in accordance with previously published protocols (30). HCA-7 cells were processed using the Direct-zol RNA extraction kit from ZymoResearch. Transcript was purified using Turbo DNase (Invitrogen, Thermo Fisher Scientific) and converted to cDNA using the High-Capacity cDNA Reverse Transcription Kit from Life Technologies, Thermo Fisher Scientific. Quantitative PCR was processed and analyzed using SYBR green and the step-one system. Fold change was assessed using the $2^{-\Delta\Delta Ct}$ method. Knockdown efficiency was confirmed by quantitative PCR using predesigned primer sets from Integrated DNA Technologies.

Claudin-2 siRNA KD. Caco-2BBe (from Robert H. Whitehead, Vanderbilt University, Nashville, Tennessee, USA) control-shRNA and TCPTP-KD cells were seeded on 12-well Transwells (0.5×10^5 cells) and grown for 7 days (30). On day 7, the medium was changed to serum-free medium. After 8 hours, cells were transfected with 50 pmol of nontargeting scrambled siRNA or 50 pmol claudin-2–specific siRNA mixed with DharmaFECT transfection reagent (Dharmacon) according to the manufacturer's instructions. In brief, per transfection, 50 pmol siRNA constructs and DharmaFECT (5 μL) were incubated separately in 50 μL serum-free DMEM for 5 minutes. The 2 mixes were combined and incubated for another 25 minutes before adding 400 μL serum-free DMEM. This mix was then used to replace the apical medium of the Caco-2BBe cell cultures. After 16 hours, basolateral and apical medium was replaced with fresh serum-free DMEM, and TER and FD4 permeability were assessed 48 hours later.

Cell fixation and immunocytochemical staining. HCA-7 and Caco-2BBe IECs were seeded on glass coverslips in 6-well MilliporeSigma plates. Media were aspirated and replaced with 1 mL of 4% PFA for 10 minutes covered from light. Four percent PFA was aspirated and wells were washed for 5 minutes (×3) with PBS. Cells were then permeabilized with 0.1% Triton X-100 solution and incubated for 10 minutes. Cells were again washed for 5 minutes (×3) with PBS. After washing, cells were treated with 50 mM of NH_4Cl for quenching (5 minutes) and washed again (5 minutes × 3) with PBS. Cells were blocked with 1% BSA in PBS for at least 15 minutes and left in 4°C until antibody incubation. Slides were probed with 1:50 dilution of primary antibodies (TCPTP, HA, matriptase, and claudin-2 from sources listed above) for 2 hours to overnight. After incubation, coverslips were washed 3 × 5 minutes with PBS and then probed with a 1:100 dilution of secondary anti-rabbit Alexa Fluor 488 antibody (Jackson ImmunoResearch) for 1 hour. Slides were washed again with PBS for 5 minutes (×3), then stained with Hoechst 33258 (MilliporeSigma) to bind DNA for visualization of the nucleus, washed again, and mounted onto slides.

Freeze fracture. Caco-2BBe cells were prepared for freeze fracture using methods similar to those previously described (69). In brief, cells were grown to confluence in 60 mm dishes and fixed with 2% glutaraldehyde in PBS for 1 hour. After fixation, cells were lifted from dishes and progressively transitioned to 30% glycerol. Samples were frozen by rapid contact with a polished gold-coated copper block cooled to –186°C using a LifeCell CF-100 "slam freezer." Freeze fracture was performed with a Balzer freeze fracture apparatus at –110°C, shadowed with platinum at a 45° angle, and stabilized with a carbon backing. The replicas were imaged using a JEOL 2100 transmission electron microscope operating at 200 kV equipped with a Gatan Orius 832 charge-coupled device camera. Strand discontinuities were characterized by comparing the number of gaps in P-face strands with their total length (calculated in 20 strand segments totaling 8–9 μm per condition).

Statistics. All statistical tests were performed using GraphPad Instat or Prism (v6) using, where appropriate, 2-tailed Student's *t* test, 1-way ANOVA or 2-way ANOVA, and Student-Newman-Keuls, Tukey's, or Bonferroni's posttest. $P \geq 0.05$ was considered not significant ($^*P \leq 0.05$; $^{**}P \leq 0.01$; $^{***}P \leq 0.001$; $^{****}P \leq 0.0001$).

Study approval. For animal studies, the experimental protocols were approved by the IACUC of UCR under protocol A-20120003B and at UCSD under protocol S02190. For human studies, the collection of intestinal biopsies, DNA preparation, and genotyping were approved by the Cedars-Sinai Medical Center Institutional Review Board (number 3358). Written informed consent was obtained from all study participants.

Author contributions

RRM, MK, MRS, and DFM designed the experiments. RRM, MK, TWP, YSP, RA, ASB, VC, MRS, LHPB, SM, EK, AS, and DFM performed the experiments. RRM, MK, RA, ASB, VC, MRS, EK, CRW, and DFM analyzed the data. CRW analyzed pathological specimens. DPBM provided human specimens. MLT provided constitutive *Tcptp*-Het mouse breeding pairs. EK and BK performed freeze fracture electron microscopy. KEB provided HT-29.cl19a cells and critical resources. EMH and LE helped develop $Ptpn2^{\Delta IEC}$ (knockout) and $Ptpn2^{fl/fl}$ mice. RRM and DFM wrote the manuscript. DFM conceived the study and obtained funding. All the authors critically reviewed and approved the final version of the manuscript. RRM, MK, and MRS share joint first authorship as RRM was the lead experimenter at the beginning of the study, MK performed critical experiments to complete the initial submission, and MRS performed critical experiments to complete extensive revisions to the study.

Acknowledgments

We are grateful to Christina Van Itallie (National Heart, Lung, and Blood Institute, NIH) and Pradipta Ghosh (UCSD) for helpful discussions regarding freeze fracture studies and to Tony Tiganis, Monash University, Australia, for the EGFP-C1-TC45 construct. Funding support: NIH 2R01DK091281, 1R01AI153314 (DFM), and DK120515 (LE); Crohn's and Colitis Foundation Senior Research Award (DFM) and Career Development Award (RRM); and ASPIRE-Pfizer IBD Research Award W1227049 (DFM). The graphical abstract was created using BioRender.com.

Address correspondence to: Declan F. McCole, Division of Biomedical Sciences, University of California, Riverside, 900 University Avenue, Riverside, California 92521, USA. Phone: 951.827.7785; Email: declan.mccole@ucr.edu.

RRM's present address is: Janssen Pharmaceuticals, La Jolla, California, USA.

MRS's present address is: Division of Gastroenterology & Hepatology, University Hospital, Zurich, Switzerland.

TWP's present address is: Department of Emergency Medicine, UC Davis Health, Sacramento, California, USA.

YSP's present address is: Department of Internal Medicine, Division of Gastroenterology, Seoul National University College of Medicine, Seoul, Korea.

RA's present address is: Cedars-Sinai Medical Center, Los Angeles, California, USA.

EK's present address is: Cell Imaging Shared Resource, Department of Cell and Developmental Biology, Vanderbilt University, Nashville, Tennessee, USA.

1. Turner JR. Intestinal mucosal barrier function in health and disease. *Nat Rev Immunol*. 2009;9(11):799–809.
2. Camilleri M. Leaky gut: mechanisms, measurement and clinical implications in humans. *Gut*. 2019;68(8):1516–1526.
3. Nusrat A, et al. Molecular physiology and pathophysiology of tight junctions. IV. Regulation of tight junctions by extracellular stimuli: nutrients, cytokines, and immune cells. *Am J Physiol Gastrointest Liver Physiol*. 2000;279(5):G851–G857.
4. Shen L, et al. Tight junction pore and leak pathways: a dynamic duo. *Annu Rev Physiol*. 2011;73:283–309.
5. Vancamelbeke M, Vermeire S. The intestinal barrier: a fundamental role in health and disease. *Expert Rev Gastroenterol Hepatol*. 2017;11(9):821–834.
6. McCole DF. IBD candidate genes and intestinal barrier regulation. *Inflamm Bowel Dis*. 2014;20(10):1829–1849.
7. Meddings J. The significance of the gut barrier in disease. *Gut*. 2008;57(4):438–440.
8. Su L, et al. Targeted epithelial tight junction dysfunction causes immune activation and contributes to development of experimental colitis. *Gastroenterology*. 2009;136(2):551–563.
9. Olson TS, et al. The primary defect in experimental ileitis originates from a nonhematopoietic source. *J Exp Med*. 2006;203(3):541–552.
10. Wyatt J, et al. Intestinal permeability and the prediction of relapse in Crohn's disease. *Lancet*. 1993;341(8858):1437–1439.
11. Turpin W, et al. Increased intestinal permeability is associated with later development of Crohn's disease. *Gastroenterology*. 2020;159(6):2092–2100.
12. Kiesslich R, et al. Local barrier dysfunction identified by confocal laser endomicroscopy predicts relapse in inflammatory bowel disease. *Gut*. 2012;61(8):1146–1153.
13. Irvine EJ, Marshall JK. Increased intestinal permeability precedes the onset of Crohn's disease in a subject with familial risk. *Gastroenterology*. 2000;119(6):1740–1744.
14. Madsen KL, et al. Interleukin-10 gene-deficient mice develop a primary intestinal permeability defect in response to enteric microflora. *Inflamm Bowel Dis*. 1999;5(4):262–270.
15. Jostins L, et al. Host-microbe interactions have shaped the genetic architecture of inflammatory bowel disease. *Nature*. 2012;491(7422):119–124.
16. Liu JZ, et al. Association analyses identify 38 susceptibility loci for inflammatory bowel disease and highlight shared genetic risk across populations. *Nat Genet*. 2015;47(9):979–986.
17. Smyth DJ, et al. Shared and distinct genetic variants in type 1 diabetes and celiac disease. *N Engl J Med*. 2008;359(26):2767–2777.
18. Glas J, et al. PTPN2 gene variants are associated with susceptibility to both Crohn's disease and ulcerative colitis supporting a common genetic disease background. *PLoS One*. 2012;7(3):e33682.
19. Cobb JE, et al. Identification of the tyrosine-protein phosphatase non-receptor type 2 as a rheumatoid arthritis susceptibility locus in europeans. *PLoS One*. 2013;8(6):e66456.
20. Marcil V, et al. Association between the PTPN2 gene and Crohn's disease: dissection of potential causal variants. *Inflamm Bowel Dis*. 2013;19(6):1149–1155.
21. Spalinger MR, et al. PTPN2 regulates interactions between macrophages and intestinal epithelial cells to promote intestinal barrier function. *Gastroenterology*. 2020;159(5):1763–1777.
22. McCole DF. Phosphatase regulation of intercellular junctions. *Tissue Barriers*. 2013;1(5):e26713.
23. Tonks NK. Protein tyrosine phosphatases: from genes, to function, to disease. *Nat Rev Mol Cell Biol*. 2006;7(11):833–846.
24. Wiede F, et al. T cell protein tyrosine phosphatase attenuates T cell signaling to maintain tolerance in mice. *J Clin Invest*. 2011;121(12):4758–4774.
25. Scharl M, et al. Protection of epithelial barrier function by the Crohn's disease associated gene protein tyrosine phosphatase n2. *Gastroenterology*. 2009;137(6):2030–2040.
26. Bohmer FD, Friedrich K. Protein tyrosine phosphatases as wardens of STAT signaling. *JAKSTAT*. 2014;3(1):e28087.
27. Coskun M, et al. Involvement of JAK/STAT signaling in the pathogenesis of inflammatory bowel disease. *Pharmacol Res*. 2013;76(1–8):S1043-6618(13)00104-7.
28. Khor B, et al. Genetics and pathogenesis of inflammatory bowel disease. *Nature*. 2011;474(7351):307–317.
29. Penrose HM, et al. Spermidine stimulates T cell protein-tyrosine phosphatase-mediated protection of intestinal epithelial barrier function. *J Biol Chem*. 2013;288(45):32651–32662.
30. Krishnan M, McCole DF. T cell protein tyrosine phosphatase prevents STAT1 induction of claudin-2 expression in intestinal epithelial cells. *Ann N Y Acad Sci*. 2017;1405(1):116–130.
31. You-Ten KE, et al. Impaired bone marrow microenvironment and immune function in T cell protein tyrosine phosphatase-deficient mice. *J Exp Med*. 1997;186(5):683–693.
32. Heinonen KM, et al. T-cell protein tyrosine phosphatase deletion results in progressive systemic inflammatory disease. *Blood*. 2004;103(9):3457–3464.
33. Shen L, et al. Myosin light chain phosphorylation regulates barrier function by remodeling tight junction structure. *J Cell Sci*. 2006;119(pt 10):2095–2106.
34. Utech M, et al. Mechanism of IFN-gamma-induced endocytosis of tight junction proteins: myosin II-dependent vacuolarization of the apical plasma membrane. *Mol Biol Cell*. 2005;16(10):5040–5052.
35. Graham WV, et al. Intracellular MLCK1 diversion reverses barrier loss to restore mucosal homeostasis. *Nat Med*. 2019;25(4):690–700.
36. Al-Sadi R, et al. Mechanism of cytokine modulation of epithelial tight junction barrier. *Front Biosci (Landmark Ed)*. 2009;14:2765–2778.
37. Kaser A, et al. Inflammatory bowel disease. *Annu Rev Immunol*. 2010;28:573–621.
38. Parlato M, et al. Loss-of-function mutation in PTPN2 causes aberrant activation of JAK signaling via STAT and very early onset intestinal inflammation. *Gastroenterology*. 2020;159(5):1968–1971.
39. Zeissig S, et al. Changes in expression and distribution of claudin 2, 5 and 8 lead to discontinuous tight junctions and barrier dysfunction in active Crohn's disease. *Gut*. 2007;56(1):61–72.
40. Rosenthal R, et al. Claudin-2, a component of the tight junction, forms a paracellular water channel. *J Cell Sci*. 2010;123(pt 11):1913–1921.
41. Gunzel D, Yu AS. Claudins and the modulation of tight junction permeability. *Physiol Rev*. 2013;93(2):525–569.
42. Furuse M, et al. Conversion of zonulae occludentes from tight to leaky strand type by introducing claudin-2 into Madin-Darby canine kidney I cells. *J Cell Biol*. 2001;153(2):263–272.
43. Zhao J, et al. Multiple claudin-claudin *cis* interfaces are required for tight junction strand formation and inherent flexibility. *Commun Biol*. 2018;1:50.
44. Buzza MS, et al. Membrane-anchored serine protease matriptase regulates epithelial barrier formation and permeability in the intestine. *Proc Natl Acad Sci U S A*. 2010;107(9):4200–4205.
45. Oberst MD, et al. HAI-1 regulates activation and expression of matriptase, a membrane-bound serine protease. *Am J Physiol Cell Physiol*. 2005;289(2):C462–C470.
46. Tsai PY, et al. IL-22 upregulates epithelial claudin-2 to drive diarrhea and enteric pathogen clearance. *Cell Host Microbe*. 2017;21(6):671–681.
47. Guan Y, et al. Redistribution of the tight junction protein ZO-1 during physiological shedding of mouse intestinal epithelial cells. *Am J Physiol Cell Physiol*. 2011;300(6):C1404–C1414.
48. Thomson A, et al. The Ussing chamber system for measuring intestinal permeability in health and disease. *BMC Gastroenterol*. 2019;19(1):98.
49. McDole JR, et al. Goblet cells deliver luminal antigen to CD103+ dendritic cells in the small intestine. *Nature*. 2012;483(7389):345–349.
50. Miller MJ, et al. Mind the GAPs: insights into intestinal epithelial barrier maintenance and luminal antigen delivery. *Mucosal Immunol*. 2014;7(3):452–454.

51. Shawki A, et al. The autoimmune susceptibility gene, *PTPN2*, restricts expansion of a novel mouse adherent-invasive *E. coli*. *Gut Microbes*. 2020;11(6):1547–1566.
52. Spalinger MR, et al. PTPN2 controls differentiation of $CD4^+$ T cells and limits intestinal inflammation and intestinal dysbiosis. *Mucosal Immunol*. 2015;8(4):918–929.
53. Wiede F, et al. PTPN2 regulates T cell lineage commitment and αβ versus γδ specification. *J Exp Med*. 2017;214(9):2733–2758.
54. Svensson MN, et al. Reduced expression of phosphatase PTPN2 promotes pathogenic conversion of Tregs in autoimmunity. *J Clin Invest*. 2019;129(3):1193–1210.
55. Hsieh WC, et al. PTPN2 links colonic and joint inflammation in experimental autoimmune arthritis. *JCI Insight*. 2020;5(20):e141868.
56. Bruewer M, et al. Interferon-gamma induces internalization of epithelial tight junction proteins via a macropinocytosis-like process. *FASEB J*. 2005;19(8):923–933.
57. Furuse M, et al. Claudin-1 and -2: novel integral membrane proteins localizing at tight junctions with no sequence similarity to occludin. *J Cell Biol*. 1998;141(7):1539–1550.
58. Garcia-Hernandez V, et al. Intestinal epithelial claudins: expression and regulation in homeostasis and inflammation. *Ann N Y Acad Sci*. 2017;1397(1):66–79.
59. Tamura A, et al. Loss of claudin-15, but not claudin-2, causes Na+ deficiency and glucose malabsorption in mouse small intestine. *Gastroenterology*. 2011;140(3):913–923.
60. Escaffit F, et al. Differential expression of claudin-2 along the human intestine: Implication of GATA-4 in the maintenance of claudin-2 in differentiating cells. *J Cell Physiol*. 2005;203(1):15–26.
61. Lameris AL, et al. Expression profiling of claudins in the human gastrointestinal tract in health and during inflammatory bowel disease. *Scand J Gastroenterol*. 2013;48(1):58–69.
62. Ahmad R, et al. Targeted colonic claudin-2 expression renders resistance to epithelial injury, induces immune suppression, and protects from colitis. *Mucosal Immunol*. 2014;7(6):1340–1353.
63. Suzuki T, et al. Interleukin-6 (IL-6) regulates claudin-2 expression and tight junction permeability in intestinal epithelium. *J Biol Chem*. 2011;286(36):31263–31271.
64. Netzel-Arnett S, et al. Matriptase protects against experimental colitis and promotes intestinal barrier recovery. *Inflamm Bowel Dis*. 2012;18(7):1303–1314.
65. el Marjou F, et al. Tissue-specific and inducible Cre-mediated recombination in the gut epithelium. *Genesis*. 2004;39(3):186–193.
66. McCole DF, et al. Epidermal growth factor partially restores colonic ion transport responses in mouse models of chronic colitis. *Gastroenterology*. 2005;129(2):591–608.
67. Huang H, et al. Fine-mapping inflammatory bowel disease loci to single-variant resolution. *Nature*. 2017;547(7662):173–178.
68. Spalinger MR, et al. PTPN2 regulates inflammasome activation and controls onset of intestinal inflammation and colon cancer. *Cell Rep*. 2018;22(7):1835–1848.
69. Van Itallie CM, et al. A complex of ZO-1 and the BAR-domain protein TOCA-1 regulates actin assembly at the tight junction. *Mol Biol Cell*. 2015;26(15):2769–2787.